

0.A Scientific Goals of the GlueX Experiment

0.A.1 Introduction

The primary goal of the GLUEX project is the definitive and detailed mapping of the spectrum of a new family of particles called *hybrid mesons*. Linearly polarized photons produced by electrons from an energy-upgraded CEBAF will be the probe used to uncover this spectrum. This experimental information is absolutely critical in finding the answer to an outstanding and fundamental questions in physics – a quantitative understanding of the confinement mechanism in quantum chromodynamics.

The spectrum of mesons and baryons uncovered during the 1960's led to the quark model within which mesons are bound states of a quark and antiquark, $q\bar{q}$, and baryons are bound states of three quarks, qqq . Further experimental work indicated that quarks are dynamical objects as well and this led to the development of quantum chromodynamics (QCD), the theory of quarks and gluons and their interactions modelled after the very successful theory of quantum electrodynamics (QED). Just as charged particles interact by the exchange of photons, quarks, with their color charge, interact by exchanging gluons. There are however important and fundamental differences between the two theories. There are three types of color charge as opposed to one kind of electrical charge. And the gluons of QCD also carry color charge and can interact with quarks and each other. In contrast, the photons of QED do not carry charge. Bound states involving quarks and gluons or quarks alone are thus possible and indeed should exist. QCD also incorporates the experimental fact that the quarks and gluons do not exist as free particles by requiring that only color singlet combinations exist as free particles in nature. In addition to the color singlet combinations $q\bar{q}$ and qqq others are possible, such as $q\bar{q}g$ (*hybrid mesons*) and gg or ggg (*glueballs*). These new states, collectively known as *gluonic excitations*, are fascinating since this is the only case of a theory in which the gauge particle is also a constituent. The analogous states in QED, like atoms of light, cannot exist. Although there is tantalizing evidence for these gluonic excitations, their spectra have not been mapped out.

The confinement of quarks and gluons within the particles of which they are the constituents is a unique feature of QCD. But a quantitative understanding of the confinement mechanism still eludes us. Theoretical progress is being made and lattice QCD, based on first-principle calculations, will ultimately be able to predict a detailed spectrum, including masses and decays, of hybrid mesons and glueballs. The experimental information about the spectrum of this new form of matter as predicted by QCD is an essential ingredient for the ultimate understanding of the confinement mechanism.

The low-lying glueball states will be searched for in the glue-rich J/ψ radiative decays as part of the planned CLEO-c project at Cornell's CESR. However the low-lying glueballs possess J^{PC} quantum numbers that are the same as $q\bar{q}$ states and therefore mixing with conventional $q\bar{q}$ mesons is possible and that can complicate glueball identification. In contrast, hybrid mesons can possess J^{PC} quantum numbers not possible for $q\bar{q}$. These *exotic hybrid mesons* thus have a *smoking gun signature*. Just as nonets of $q\bar{q}$ mesons made of the three light quarks (u , d and s) exist, nature should also reveal nonets of hybrids with the same flavor quantum numbers but with now with the possibility of exotic J^{PC} . Hybrid mesons should also have widths comparable to conventional mesons. This is supported by theoretical considerations and by the possible sighting of an exotic hybrid in π^- -induced interactions.

Hybrid mesons can be thought of as $q\bar{q}g$ bound states in which the gluon is a constituent. An attractive alternative picture is one in which a gluonic flux tube forms between the q and \bar{q} in a meson. This flux tube forms because of the self-interaction of the gluons and qualitatively accounts for confinement. It leads to a linear potential, or a force that is constant as the distance between the quark and anti-quark varies. Infinite energy is required to separate the quarks to infinity, thus qualitatively accounting for confinement. This notion of a relativistic string or flux tube between the quarks was introduced in the 1970's to account for the observed linear dependence of particle mass-squared (m^2) on spin (J). The flux tube concept is supported by lattice QCD studies. Within this picture conventional mesons result when the flux tube is in its ground state. Hybrid mesons arise when the flux tube is excited. The lack of information on this spectroscopy is due in part to the complicated decay modes favored by these states and also due to the apparent suppression of exotic hybrid mesons in production mechanisms with π or K probes. On the other hand production of exotic hybrid mesons is expected to be favored using beams of photons and essentially no data exist on the photoproduction of light mesons. The GLUEX project will remedy this situation.

In addition to providing for a linearly polarized photon beam of sufficient energy, the GLUEX project includes construction of a hermetic detector to allow for particle identification and momentum and energy determination sufficient to allow for complete kinematic reconstruction of events with a wide variety of final states. This is essential for the spin analysis – partial wave analysis (PWA) – needed to determine the J^{PC} quantum numbers, to map out the flavor quantum numbers of the hybrid nonets and to test assumptions about the details of confinement that would lead to predicting specific decay modes.

In this chapter we expand on the following:

1. *Spectroscopy of Light Mesons*. This will include a brief review of the conventional

quark model and the status of the light quark meson spectrum.

2. *Gluonic excitations and the role in QCD.* This will include a discussion of how the gluons form flux tubes, and how their excitations lead to QCD mesons, in particular exotic hybrids. This general picture is not restricted to a particular model but follows from the first-principles QCD calculations.
3. *The current evidence for gluonic excitations.* The evidence comes from overpopulation of conventional nonets and from possible glueball and exotic hybrid sightings in $\bar{p}p$ annihilations and π -induced interactions.
4. *Photons are expected to be particularly effective in producing exotic hybrids.* Its spin structure makes the photon a qualitatively different probe from π and K beams. The first excited transverse modes of the flux tube can lead to exotic hybrids only when the quark spins are aligned. This argument is consistent with expectations from models based on phenomenological analyses of existing data that predict cross sections for photoproduction of exotic hybrids comparable to those of normal mesons. And there are essentially no data on photoproduction of light mesons so this is *terra incognita*. The existing photoproduction data will be discussed.
5. *The complementarity of this study with other planned projects that will study gluonic excitations.* We will compare this to searches in the charm quark or beauty quark sectors or e^+e^- annihilations, in particular the GSI Project and the CLEO-c Project at Cornell.
6. *The importance of the PWA technique in uncovering exotic mesons.* The PWA is a powerful analysis tool that has been successfully employed in experiments to uncover states which are not evident from a simple examination of mass spectra (bump-hunting). PWA is absolutely essential for this project as is the development of the formalism for incident photon beams and an understanding of the phenomenology. The importance of a hermetic detector with excellent resolution and rate capability and sensitivity to a wide variety of decay modes will be discussed.
7. *Linear polarization of the photon beam is essential for this study.* Linear polarization is important in the determination of the J^{PC} quantum numbers and it is essential in determining the production mechanism. Linear polarization can be used as a filter for exotics once the production mechanism is isolated.
8. *The ideal photon energy range.* In order to reach the desired mass range we need to be far enough above threshold so that the decay products of produced mesons can be detected and measured with sufficient precision. High enough energies are also important to avoid line-shape distortions of higher-mass mesons. We also want to be

high enough in energy to kinematically separate production of baryon resonances from production of meson resonances. This need for higher energies, however is balanced by the need to limit the maximum energy to allow for a solenoid-only-based detector to accurately determine the momenta of the highest energy charged particles. These considerations lead to an ideal photon energy in the range from 8 to 9 GeV .

9. *The desired electron energy.* Having established the desired photon beam energy of 9 GeV the electron energy must be sufficiently high compared to the desired photon beam energy to achieve a sufficient degree of linear polarization. With 12 GeV electrons, the degree of linear polarization is 40%. If the electron energy drops to 10 GeV the degree of polarization drops to 5%. The ratio of tagged hadronic rate to total hadronic rate in the detector drops as the electron energy approaches the desired photon energy. The conclusion is that an electron energy of 12 GeV suffices but lower energies will severely compromise the physics goals.

0.A.2 Conventional light mesons

The early version of the quark model described the observed mesons as bound states of a quark and antiquark, where the quarks were assumed to be the u , d and s quarks. Thus mesons were grouped in families with nine members – a nonet – characterized by a given J^{PC} determined by the relative spin of the two quarks and their relative orbital angular momentum. Within the nonet three are members of an isotriplet with zero strangeness. Two are members of an isodoublet with positive strangeness and another two with negative strangeness. And the remaining two members have zero strangeness and isospin. This flavor pattern holds for all the nonets. Radial excitations are also allowed.

The rules for allowed values of J^{PC} follow from the requirements of a fermion–antifermion system: the quark spins can be parallel ($S = 1$) or antiparallel ($S = 0$) with relative orbital angular momentum (L), $\vec{J} = \vec{L} + \vec{S}$, $P = (-1)^{L+1}$ and $C = (-1)^{L+S}$. Thus the low-lying nonet with $\vec{L} = 0$ and $\vec{S} = 0$ leads to $J^{PC} = 0^{-+}$, the pseudoscalar nonet, including the π , K , η and η' mesons. The nonet with $\vec{L} = 0$ and $\vec{S} = 1$ leads to $J^{PC} = 1^{--}$, the vector mesons, including the ρ , K^* , ω and ϕ mesons. The combination $\vec{L} = 1$ and $\vec{S} = 1$ leads to three nonets: scalar ($J^{PC} = 0^{++}$), axial vector ($J^{PC} = 1^{++}$) and tensor ($J^{PC} = 2^{++}$).

Using the rules for determining J^{PC} for a fermion-antifermion system, certain J^{PC} combinations are not allowed for $q\bar{q}$ systems and these include $J^{PC} = 0^{--}$, 0^{+-} , 1^{-+} , 2^{+-} , \dots . Such combinations are referred to as *exotic* quantum numbers. Indeed, that such combinations were not initially observed gave credence to the quark model.

Figure 1 shows our current knowledge of conventional $q\bar{q}$ states. The exact association of an observed meson with a particular $q\bar{q}$ state within a nonet depends on a good understanding of the various decay modes of the meson as well as its mass, width and production characteristics. Figure 1 also shows the expected range of masses for glueballs, hybrid mesons and meson-meson molecular states. These will be described in more detail below.

The range of masses of the known conventional meson nonets and their radial excitations extend from the π mass up to about $2.5 \text{ GeV}/c^2$. Figure 2 shows the spectrum of $q\bar{q}$ states in more detail including radial excitations. There is also now clear evidence that the observed meson spectrum includes states which cannot be accommodated within the naive quark model. For example, there are at least five scalar states reported with masses below $2 \text{ GeV}/c^2$. These, along with indications of exotic J^{PC} sightings will be discussed below.

0.A.3 Gluonic excitations and confinement

The Standard Model of elementary particles includes the electroweak theory and QCD, the latter describing the strong interactions among the quarks and gluons. At short distances – the regime of asymptotic freedom – perturbative techniques are applicable and QCD describes high energy experimental phenomena both qualitatively and quantitatively. At large distance scales – the confinement regime – the situation is far different. Here the successful calculational techniques of the perturbative regime cannot be used. We must rely on first-principles lattice QCD calculations or QCD-inspired models. There has been significant theoretical effort in this area recently and more progress can be expected in the near future, especially as multi-teraflop lattice QCD centers come into operation.

Understanding confinement in QCD requires a detailed understanding of the role of gluons. QCD is distinct from QED in that the force carriers of the former (gluons) carry color charge whereas for the latter the photons are electrically neutral. As illustrated in Figure 3, the force between two electrically charged particles falls off like the inverse square of the distance between the charges. The number of field lines intersecting a unit area midway between the charges and perpendicular to the line connecting them would decrease as the inverse square of the distance between the charges. In contrast, the color field lines between a quark and an anti-quark do not fill all of space as in the case with electrical charges. Rather the field lines form flux tubes. A unit area placed midway between the quarks and perpendicular to the line connecting them intercepts a constant number of field lines, independent of the distance between the quarks. This leads to a constant force between the quarks – and a large force at that, equal to about 16 metric

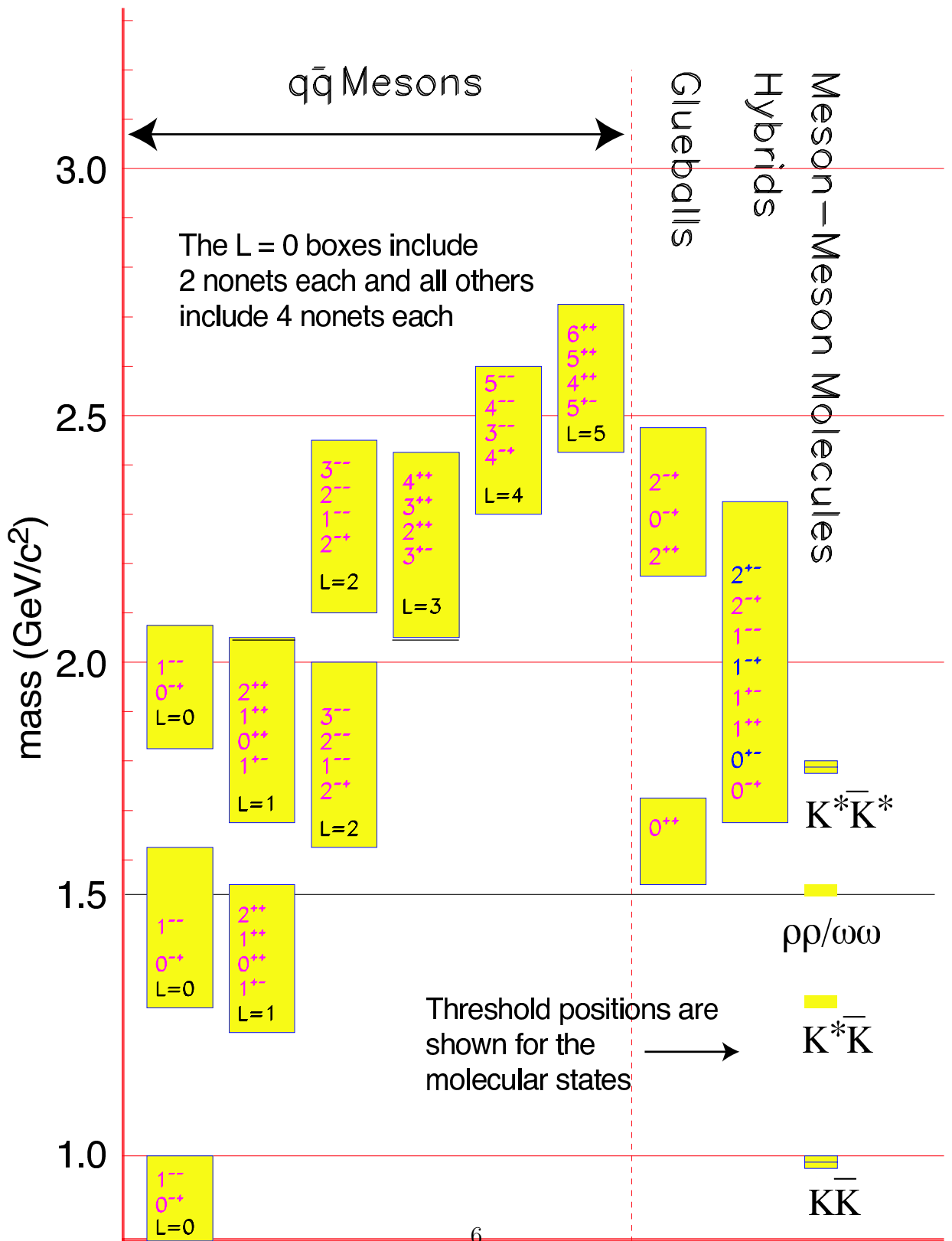


Figure 1: A level diagram showing conventional nonets and expected masses of glueballs, hybrids and molecular thresholds. The vertical axis is in units of GeV/c^2 . For the $q\bar{q}$ boxes the L refers to the angular momentum between the quarks and each J^{PC} refers to a nonet of mesons. Note also that exotic J^{PC} , -0^{+-} , 1^{-+} , 2^{+-} – occur only among the hybrids for the range of masses shown.

Light Quark Mesons

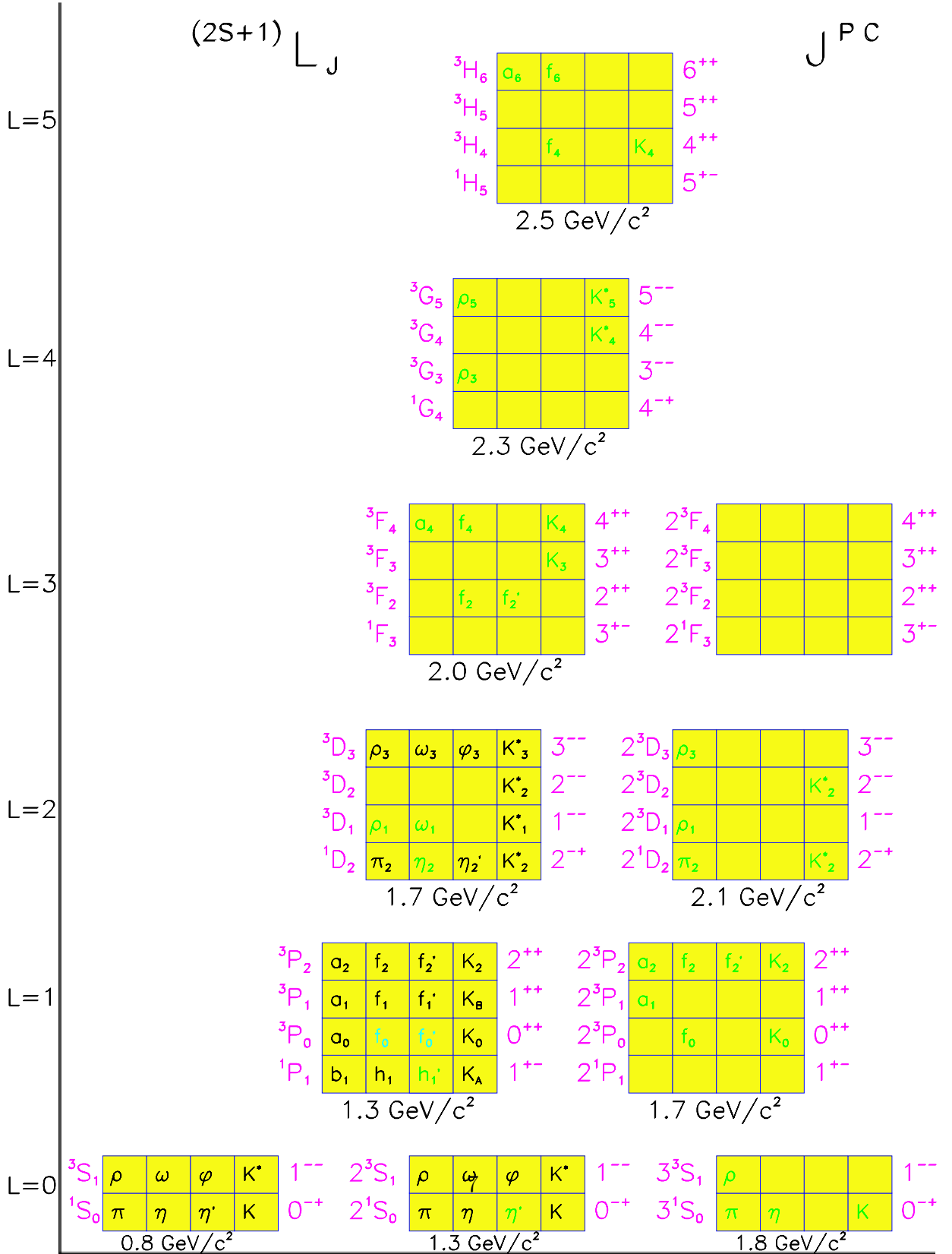


Figure 2: The $q\bar{q}$ spectrum of states. The assignments of the light colored states are speculative, while the empty boxes are missing states. The orbital angular momentum of

tons. The potential associated with this constant force is linear and grows with increasing distance. It takes infinite energy to separate the quarks to infinity and thus, qualitatively at least, this accounts for confinement.

Lattice QCD calculations support this notion of the formation of a flux tube between the quark and anti-quark. Figure 4 shows the energy density in the color field between a quark and an anti-quark in a meson with a separation of $1.2 fm$. The density peaks at the positions of the quarks and is confined to a tube between the quarks. This calculation is for heavy quarks in the quenched approximation. Figure 4 also shows the corresponding potential between the quarks. The ground state potential has a $1/r$ dependence at small distances and is linear for large distances.

This notion of the formation of flux tubes was first introduced in the 1970's by Yoichiro Nambu [Na70] to explain the observed linear Regge trajectories – the linear dependence of mass squared, m^2 , of hadrons on their spin, J . This linear dependence results if one assumes that massless quarks are tied to the ends of a relativistic string with constant mass (energy) per length with the system rotating about its center. The linear m^2 versus J dependence only arises when the mass density per length is constant, which is equivalent to a linear potential.

Within this picture, conventional mesons arise when the flux tube is in its ground state. Excitations of the flux tube lead to hybrid mesons that exhibit both the quark and gluonic degrees of freedom. The first excited state of the flux tube is a transverse excitation. The flux tube, or string, spins clockwise or counter-clockwise around the $q\bar{q}$ line leading to two degenerate states – degenerate since the energy should not depend on which way the flux tube is spinning. Lattice QCD and flux tube models both indicate that the lowest excited flux tube has $J = 1$ [Be96, Ik85, La97]. The linear combinations of the clockwise or counter-clockwise rotations are eigenstates of parity and charge conjugation leading to two possibilities for the excited flux tube: $J^{PC} = 1^{-+}$ or $J^{PC} = 1^{+-}$. Suppose we start with the $q\bar{q}$ in the $S = 0$ and $L = 0$ (or $J^{PC} = 0^{-+}$ – the π or K) configuration. Combining this with $J^{PC} = 1^{-+}$ or $J^{PC} = 1^{+-}$ of the excited flux tube results in hybrid mesons with $J^{PC} = 1^{++}$ or $J^{PC} = 1^{--}$. These are non-exotic quantum numbers. If, however, we start with $q\bar{q}$ in the $S = 1$ and $L = 0$ (or $J^{PC} = 1^{--}$ – the vector photon) configuration, the resulting hybrid meson can have $J^{PC} = [0, 1, 2]^{+-}$ for the flux tube with $J^{PC} = 1^{-+}$ and $J^{PC} = [0, 1, 2]^{-+}$ for the flux tube with $J^{PC} = 1^{+-}$. We note that of these six possible J^{PC} combinations, three are exotic: $J^{PC} = 0^{+-}$, $J^{PC} = 1^{-+}$ and $J^{PC} = 2^{+-}$. These states will not mix with $q\bar{q}$ and thus have unique signatures.

Meson production proceeds with an incoming probe interacting with the target particle and one result of the scattering can be the excitation of the flux tube. If the probe

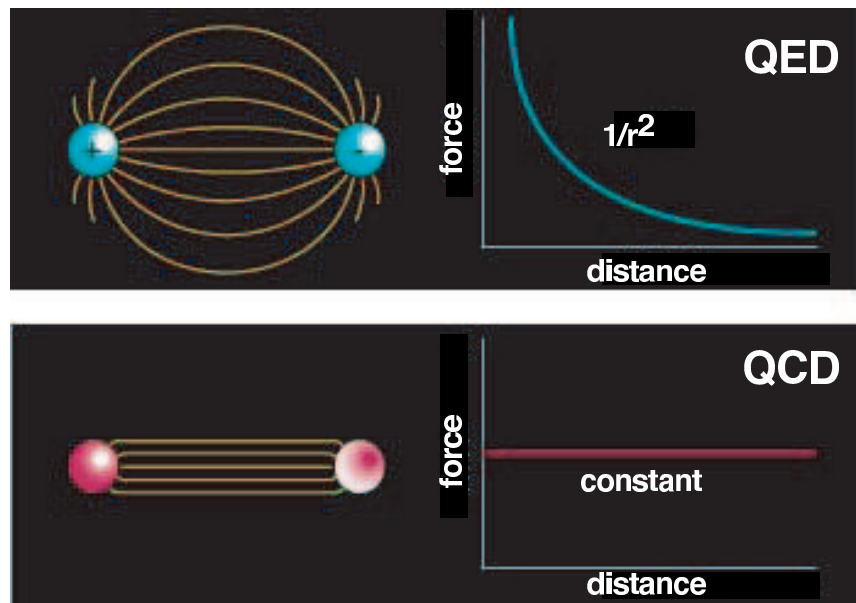


Figure 3: Field lines associated with the electrical force between two electrically charged particles (top) and the corresponding dependence of force on the distance between the charges and the field lines associated with the color force (bottom) between two quarks and the corresponding dependence of force on distance.

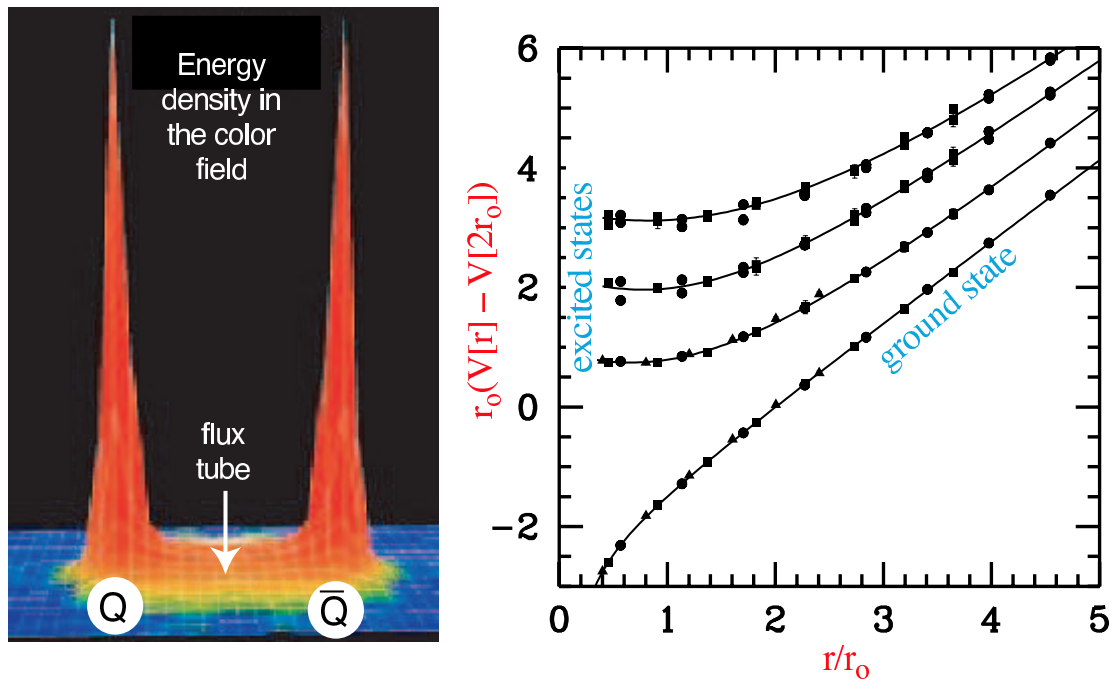


Figure 4: (left) A lattice QCD calculation of the energy density in the color field between a quark and an anti-quark. The density peaks at the positions of the quarks and is confined to a tube between the quarks. This calculation is for heavy quarks in the quenched approximation. (right) The corresponding potential between the quarks. The ground state potential has a $1/r$ dependence at small distances and is linear for large distances.

is a $q\bar{q}$ in $L = 0$ and $S = 0$ (π or K), production of exotic hybrids will not be favored. But if the $q\bar{q}$ probe has $L = 0$ and $S = 1$, for example a photon, one expects exotic hybrids to be produced readily.

Finally we consider the expected masses for hybrid mesons. We would expect the mass difference between the ground state (conventional) mesons and hybrid mesons to be given by the level spacing between the ground state of the flux tube and the first excited transverse mode and that is simply given by π/r where r is the quark separation. When translated to appropriate units this corresponds to about $1 \text{ GeV}/c^2$.

In this discussion the motion of the quarks was ignored, but we know from general principles [Is85] that an approximation that ignores the impact of the flux tube excitation and quark motion on each other seems to work quite well.

0.A.4 Observation of gluonic excitations

Glueballs

Lattice QCD calculations indicate that lightest glueball is a scalar with a mass in the range from 1.5 to $1.7 \text{ GeV}/c^2$ [Mo97, Ba93, Se95, Ba98]. Indeed there is evidence from the Crystal Barrel experiment, which studied $\bar{p}p$ annihilations at CERN, that the $f_0(1500)$ is a leading candidate for a glueball [Am95, Am96]. There are, however, indications that this state is not a pure glueball but has some mixing with conventional $q\bar{q}$ [Cl01]. There are also strong indications that the scalar meson sector contains one or more glueballs since there are several more observed states than can be accommodated in the simple $q\bar{q}$ model. However, the unique identification of a glueball is exacerbated by the possibility of mixing with $q\bar{q}$. Lattice QCD indicates a rich spectrum of glueballs, all with non-exotic quantum numbers, from 1.5 to $2.5 \text{ GeV}/c^2$. The lightest glueball with exotic quantum numbers is predicted to have $J^{PC} = 2^{+-}$ and to have a mass of $4 \text{ GeV}/c^2$ [Mo97].

Exotic hybrid mesons

After about two decades of experimental searches there have been reports of experimental observations of states with exotic $J^{PC} = 1^{-+}$ by the Brookhaven E852 collaboration in π^-p interactions at $18 \text{ GeV}/c$. One of these has a mass of $(1593 \pm 8_{-47}^{+29}) \text{ MeV}/c^2$ and width of $(168 \pm 20_{-12}^{+150}) \text{ MeV}/c^2$ and decays into $\rho^0\pi^-$ [Ad98]. This state was observed in the reaction $\pi^-p \rightarrow \pi^+\pi^-\pi^-p$ at a beam momentum of $18 \text{ GeV}/c$. In Figure 5, the acceptance-corrected (average acceptance was 25%) distributions of the $\pi^+\pi^-\pi^-$ and $\pi^+\pi^-$ effective masses are shown. The positions of well-established meson states are shown, including the $a_1(1260)$, which does not show up as a prominent peak in the overall mass distribution.

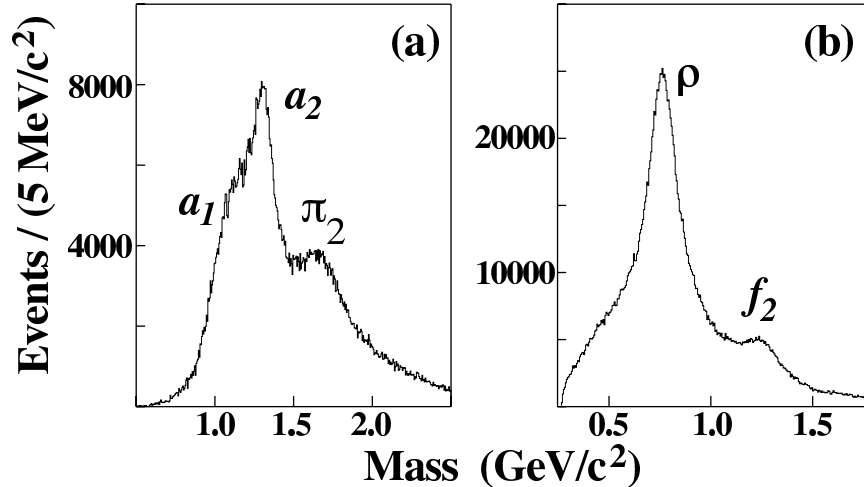


Figure 5: Acceptance corrected effective mass distributions for the (a) $\pi^+\pi^-\pi^-$ combination and (b) $\pi^+\pi^-$ combination (two entries per event) from E852 [Ad98].

The partial wave analysis (PWA) performed on these data assumes an *isobar model* – a parent decaying into a $\pi\pi$ state and an unpaired π followed by the decay of the $\pi\pi$ state. The resulting decomposition into various waves is shown in Figure 6. The decomposition clearly shows the $\pi(1800)$ in the 0^{-+} wave, the $a_1(1260)$ in the 1^{++} wave, the $\pi_2(1670)$ in the 2^{-+} wave, and the $a_2(1320)$ in the 2^{++} wave. Evidence for the exotic 1^{-+} $\rho\pi$ is shown in Figure 7. If an isovector $\rho\pi$ resonates in an $L = 1$ wave, it has $J^{PC} = 1^{-+}$. Also shown in this figure is the effect of leakage of non-exotic waves. Finally in Figure 8 a coupled fit to the wave intensities and phase difference between the 1^{-+} and 2^{-+} waves is shown.

Another state reported by E852 has a similar mass, $(1597 \pm 10_{-10}^{+45}) \text{ MeV}/c^2$, but with a significantly larger width, $(340 \pm 40_{-50}^{+50}) \text{ MeV}/c^2$, and decays into $\eta'\pi^-$ [Iv01]. It has not been determined whether these represent two decay modes of the same state or whether they are due to two different mechanisms.

The E852 collaboration also reported observation of another $J^{PC} = 1^{-+}$ state with mass $(1370 \pm 16_{-30}^{+50}) \text{ MeV}/c^2$ and a width of $(385 \pm 40_{-105}^{+65}) \text{ MeV}/c^2$ decaying into $\eta\pi^-$ [Th97]. If an $\eta\pi$ system is in a P wave, the resulting J^{PC} quantum number combination is exotic (1^{-+}). In these studies the dominant state observed in the $\eta\pi$ channel is the $J^{PC} = 2^{++}$ $a_2(1320)$ seen in the D -wave. Critical to the identification of this state is not only showing the presence of a P -wave, but also that the resulting line shape is consistent with a Breit-Wigner and that the phase motion of the P , as determined by its interference with the dominant D -wave, cannot be due solely to the $a_2^-(1320)$ resonance. Soon after the E852 report, the Crystal Barrel Collaboration reported an exotic $J^{PC} = 1^{-+}$ state

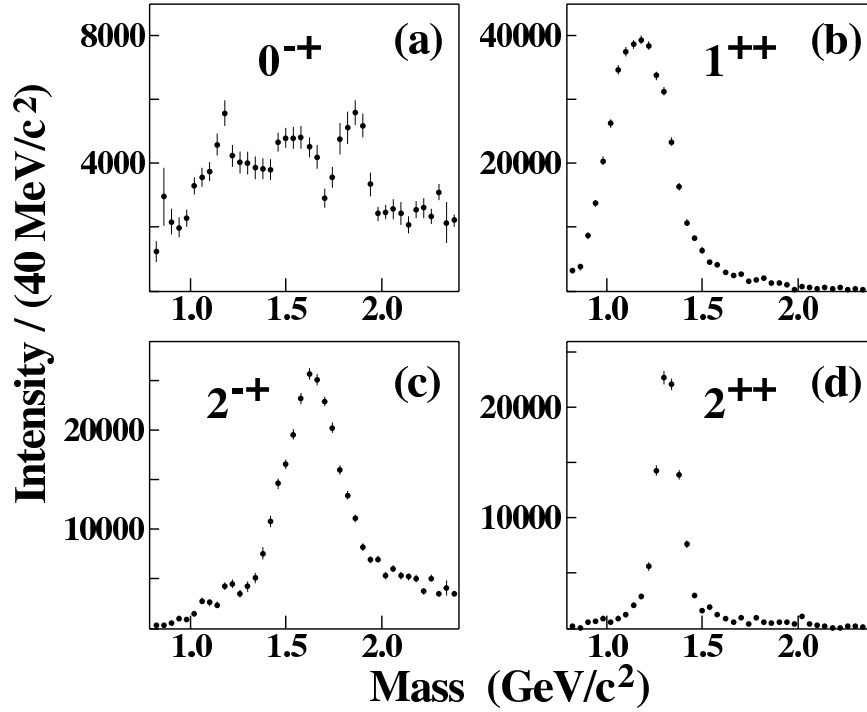


Figure 6: Combined intensities for all (a) 0^{-+} waves; (b) 1^{++} waves; (c) 2^{-+} waves; and (d) 2^{++} waves from E852 [Ad98].

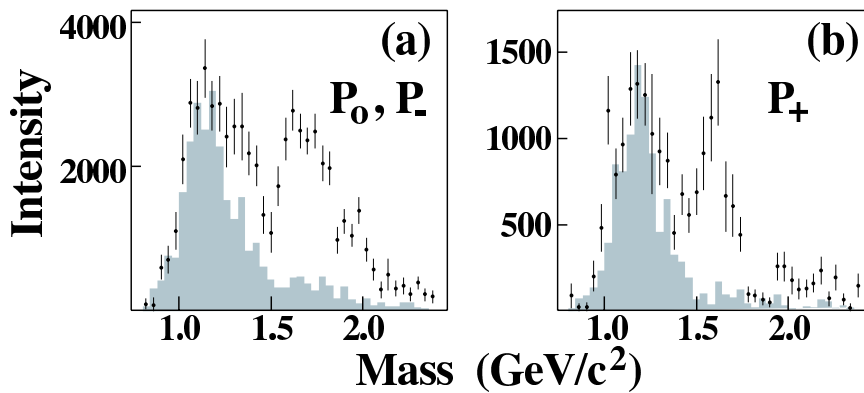


Figure 7: The intensities for the waves corresponding to 1^{-+} into $\rho\pi$. The shaded distributions are an estimate of leakage due to non-exotic waves – from E852 [Ad98].

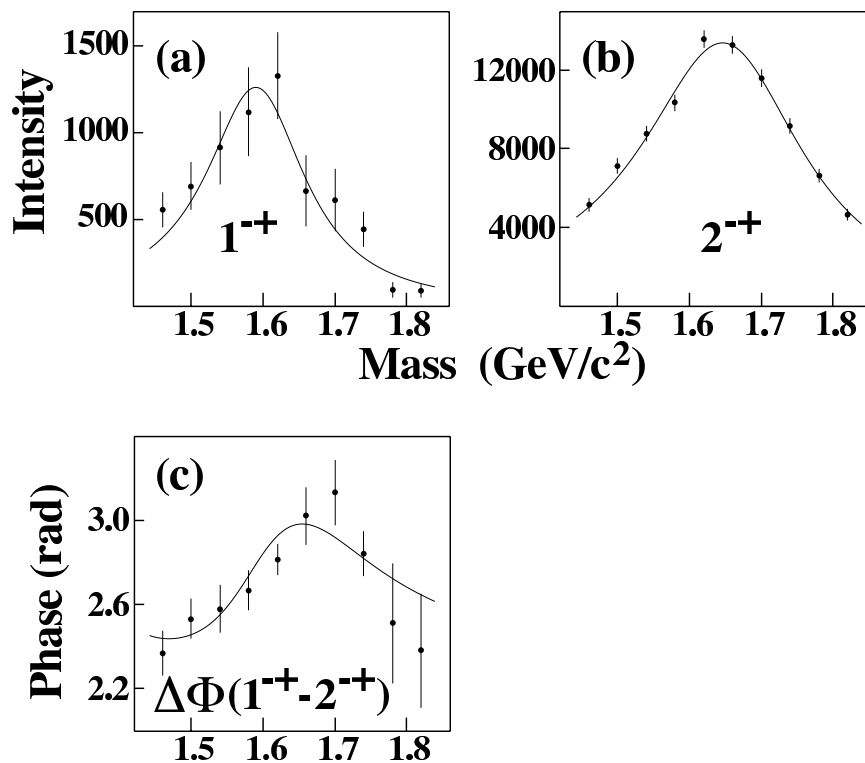


Figure 8: Results of a coupled mass-dependent Breit-Wigner fit of the 1^{-+} and 2^{-+} waves showing the phase difference as well – from E852 [Ad98].

produced in $\bar{p}n \rightarrow \pi^-\pi^0\eta$ obtained by stopping antiprotons in liquid deuterium [Ab98]. They reported a mass of $(1400 \pm 20_{-20}^{+20}) \text{ MeV}/c^2$ and a width of $(310 \pm 50_{-30}^{+50}) \text{ MeV}/c^2$.

The first claim of an exotic meson decaying into $\eta\pi^0$ with a mass of $1400 \text{ MeV}/c^2$ was made by the GAMS collaboration in the reaction $\pi^-p \rightarrow \eta\pi^0n$ [Al88] but a later analysis by the group [Yu95] led to ambiguous results. The VES collaboration also presented evidence for a P-wave contribution in $\eta\pi$ [Be93] and at KEK a claim was made for an exotic $\eta\pi$ state [Ao93] as well, but with a mass and width close to that of the $a_2(1320)$; leakage from the dominant D wave could not be excluded.

In all the observations in π -induced reactions, the $\eta\pi$ P -wave enhancements have cross sections that are substantially smaller than the dominant $a_2(1320)$ so leakage, usually due to an imperfect understanding of experimental acceptance, is a source of concern. In contrast, the observed yield of the $\pi_1(1400)$ yield in $\bar{p}p$ annihilations is of the same magnitude as the $a_2(1320)$. Apart from these experimental issues, the interpretation of the nature of low-mass $\eta\pi$ P -wave amplitude and phase motion should be guided by the principle of parsimony – less exotic interpretations must also be considered. In a recent analysis of the $\eta\pi^0$ system in the reaction $\pi^-p \rightarrow \eta\pi^0n$ from data using the E852 apparatus, a P -wave is observed but it is not consistent with a Breit-Wigner resonance. The observed P -wave phase motion is consistent with $\eta\pi^0$ final state interactions. This could explain the relatively wide width of the observed $\eta\pi^-$ state and could also explain the broad $\eta'\pi^-$ enhancement. The $\pi^-p \rightarrow \eta\pi^0n$ and $\pi^-p \rightarrow \eta\pi^-p$ have some notable differences. For the former charge conjugation (C) is a good quantum number but not for the latter and for the former both the $a_0(980)$ and $a_2(1320)$ are prominently present but for the latter only the $a_2(1320)$ is strongly produced. This is an important factor in selecting the physical solutions among mathematically ambiguous solutions.

The conclusion from these studies is that there indeed are tantalizing hints of gluonic excitations in both the glueball and hybrid sectors but the results are not conclusive. The large statistics samples of high quality data to be collected with the GLUEX detector will provide the definite resolution of the murky situation. Furthermore there is good reason to believe that whereas exotic hybrids may be suppressed in π production, they are enhanced in photoproduction where essentially no data exist. In the glueball sector, the large samples of glue-rich radiative J/ψ decays should shed light on the spectrum of these gluonic excitations.

0.A.5 Photoproduction of exotic hybrids

Why photoproduction?

Based on the arguments presented above, the photon is expected to be particularly effective in producing the *smoking gun* signature for gluonic excitations: hybrids with exotic J^{PC} . In this regard, we will compare the effectiveness of the π or K as a probe with that of the photon. In the former case, the meson is a $q\bar{q}$ with spins anti-aligned ($S = 0$) and in the latter, the photon is a virtual $q\bar{q}$ with spins aligned ($S = 1$). In both cases, the relative orbital angular momentum is zero ($L = 0$) and the flux tube connecting the quarks is in its ground state. Figure 9 illustrates the differences between a π probe and a γ probe. If the scattering results in excitation of the flux tube, one expects exotic hybrid mesons to be suppressed in π -induced interactions and enhanced in photoproduction.

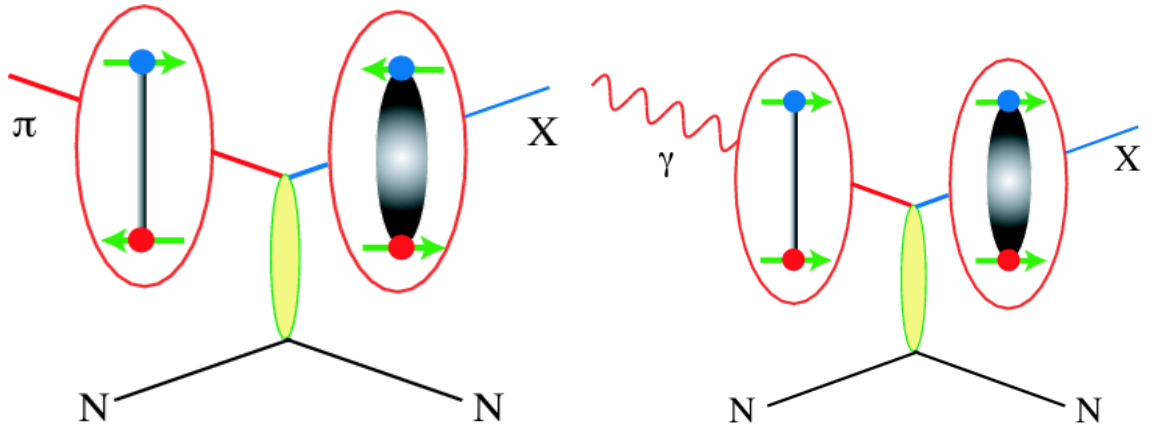


Figure 9: (left) With a π probe the incoming quarks have $L = 0$ and $S = 0$. The excited flux tube from the scattering results in hybrid mesons with non-exotic quantum numbers. (right) With a photon probe the incoming quarks have $L = 0$ and $S = 1$. When the flux tube is excited, hybrid mesons with exotic quantum numbers are possible.

Current phenomenology also supports the notion that photons should be more effective at producing exotic hybrids [Af98, Sz01]. Figure 10 shows an estimate of the photoproduction cross sections at 8 GeV for the $a_2(1320)$ and the exotic $\pi_1(1600)$ [Sz01]. The model uses as input the ratio of $\pi_1(1600)$ to $a_2(1320)$ as observed in E852. The model is compared with photoproduction of the $a_2(1320)$ at 5 GeV . Whereas in E852, with a π beam, the $\pi_1(1600)$ is produced at about 5% of the rate for $a_2(1320)$, in photoproduction the rates for $\pi_1(1600)$ are expected to be comparable for that of the $a_2(1320)$. In the case of the incident π , the $\pi_1(1600)$ is produced by ρ exchange and the suppression at very low- $|t|$ due to angular momentum – spin 0 in and spin 1 out – decreases the cross section. This is to be compared to photoproduction of the $\pi_1(1600)$ with π exchange where there is no

suppression at very low- $|t|$ since now we have spin 1 in and spin 1 out. Furthermore the $N\rho N$ coupling at the baryon vertex in the incident π case is lower by a factor of 4 compared to the $N\pi N$ in the photoproduction case.

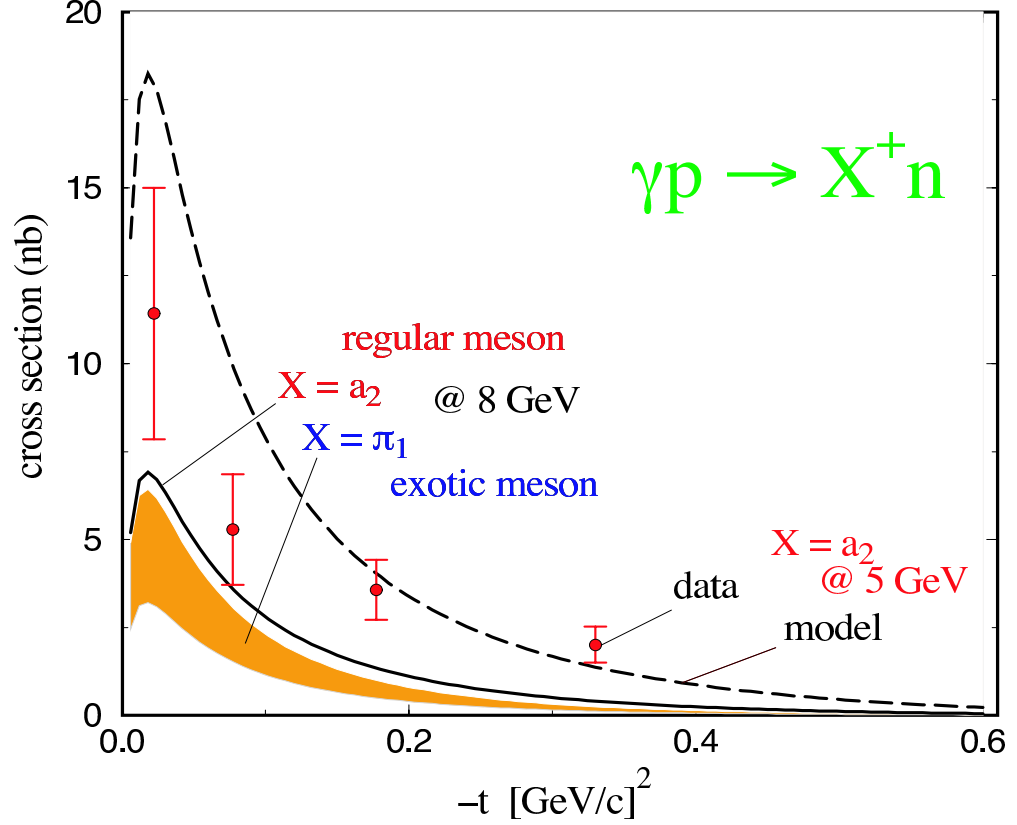


Figure 10: Estimates of the photoproduction cross sections for $a_2(1320)$ and the exotic $\pi_1(1600)$ at 8 GeV based on a phenomenological analysis described in [Sz01]. The model uses as input the ratio of $\pi_1(1600)$ to $a_2(1320)$ as observed in E852. The model is compared with photoproduction of the $a_2(1320)$ at 5 GeV .

To underscore the differences between existing photoproduction and π production, the corresponding largest data sets on 3π production are compared in the plots of Figure 11. The 3π mass spectrum from the reaction $\pi^- p \rightarrow \pi^+ \pi^- \pi^- p$ at 18 GeV/c from E852 at Brookhaven is shown. Also shown is the 3π mass spectrum from the reaction $\gamma p \rightarrow \pi^+ \pi^+ \pi^- n$ at 19 GeV from SLAC. We note the large difference in statistics between the two and we also note the differences in the structure of the spectra.

Reaction	E_γ GeV	σ (μb)	Events	Ref.
$\gamma p \rightarrow p\pi^+\pi^-$	9.3		3500	[Ba73]
$\gamma p \rightarrow p\pi^+\pi^-$	19.3		20908	[Ab94]
$\gamma p \rightarrow p\pi^+\pi^-\pi^0$	2.8		2159	[Ba73]
$\gamma p \rightarrow p\pi^+\pi^-\pi^0$	4.7		1606	[Ba73]
$\gamma p \rightarrow p\pi^+\pi^-\pi^0$	9.3		1195	[Ba73]
$\gamma p \rightarrow p\pi^+\pi^-\pi^0$	4.7–5.8	$13.5 \pm 1.5 \mu\text{b}$	3001	[Ei72]
$\gamma p \rightarrow p\pi^+\pi^-\pi^0$	6.8–8.2	$11.8 \pm 1.2 \mu\text{b}$	7297	[Ei72]
$\gamma p \rightarrow n\pi^+\pi^+\pi^-$	4.7–5.8	$4.6 \pm 1.4 \mu\text{b}$	1723	[Ei72]
$\gamma p \rightarrow n\pi^+\pi^+\pi^-$	6.8–8.2	$4.0 \pm 1.2 \mu\text{b}$	4401	[Ei72]
$\gamma p \rightarrow n\pi^+\pi^+\pi^-$	16.5–20		3781	[Co93]
$\gamma p \rightarrow p\pi^+\pi^-\pi^0$	20–70		14236	[At84]
$\gamma p \rightarrow p\pi^+\pi^-\pi^+\pi^-$	4–6	$4.0 \pm 0.5 \mu\text{b}$	~ 330	[Da73]
$\gamma p \rightarrow p\pi^+\pi^-\pi^+\pi^-$	6–8	$4.8 \pm 0.5 \mu\text{b}$	~ 470	[Da73]
$\gamma p \rightarrow p\pi^+\pi^-\pi^+\pi^-$	8–12	$4.5 \pm 0.6 \mu\text{b}$	~ 470	[Da73]
$\gamma p \rightarrow p\pi^+\pi^-\pi^+\pi^-$	12–18	$4.4 \pm 0.6 \mu\text{b}$	~ 380	[Da73]
$\gamma p \rightarrow p\pi^+\pi^-\pi^+\pi^-$	15–20		6468	[Ab85]
$\gamma p \rightarrow p\pi^+\pi^-\pi^0\pi^0$	20–70		8100	[At84a]
$\gamma p \rightarrow p\pi^+\pi^+\pi^-\pi^-\pi^0$	19.5		2553	[Bl97]
$\gamma p \rightarrow \Delta^{++}\pi^-\pi^+\pi^-$	4–6	$1.65 \pm 0.2 \mu\text{b}$	~ 200	[Da73]
$\gamma p \rightarrow \Delta^{++}\pi^-\pi^+\pi^-$	6–8	$1.8 \pm 0.2 \mu\text{b}$	~ 200	[Da73]
$\gamma p \rightarrow \Delta^{++}\pi^-\pi^+\pi^-$	8–12	$1.1 \pm 0.2 \mu\text{b}$	~ 200	[Da73]
$\gamma p \rightarrow \Delta^{++}\pi^-\pi^+\pi^-$	12–18	$1.15 \pm 0.2 \mu\text{b}$	~ 200	[Da73]
$\gamma p \rightarrow p\omega$	4.7–5.8	$2.3 \pm 0.4 \mu\text{b}$	< 1600	[Ei72]
$\gamma p \rightarrow p\omega$	6.8–8.2	$2.0 \pm 0.3 \mu\text{b}$	< 1200	[Ei72]
$\gamma p \rightarrow p\omega$	4.7	$3.0 \pm 0.3 \mu\text{b}$	1354	[Ba73]
$\gamma p \rightarrow p\omega$	9.3	$1.9 \pm 0.3 \mu\text{b}$	1377	[Ba73]
$\gamma p \rightarrow p\phi$	4.7	$0.41 \pm 0.09 \mu\text{b}$	136	[Ba73]
$\gamma p \rightarrow p\phi$	9.3	$0.55 \pm 0.07 \mu\text{b}$	224	[Ba73]
$\gamma p \rightarrow na_2^+$	4.7–5.8	$1.7 \pm 0.9 \mu\text{b}$		[Ei72]
$\gamma p \rightarrow na_2^+$	6.8–8.2	$0.9 \pm 0.9 \mu\text{b}$		[Ei72]
$\gamma p \rightarrow na_2^+$	19.5	$0.29 \pm 0.06 \mu\text{b}$	~ 100	[Co93]

Table 1: A sample of measured photoproduction cross sections from several references. Note the small numbers of events in any given channel.

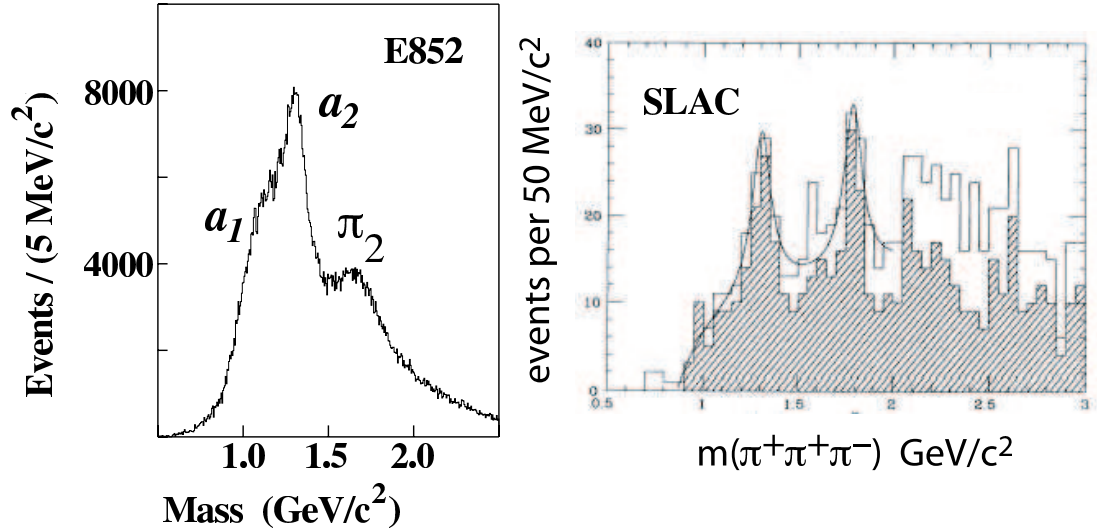


Figure 11: (left) The 3π mass spectrum from the reaction $\pi^- p \rightarrow \pi^+ \pi^- \pi^- p$ at 18 GeV/c from E852 at Brookhaven. (right) The 3π mass spectrum from the reaction $\gamma p \rightarrow \pi^+ \pi^+ \pi^- n$ at 19 GeV from SLAC.

Current photoproduction data

Table 1 is a partial compilation of known photoproduction cross sections and the numbers of events from the existing experiments. The typical cross sections range from of order $0.1 \mu b$ up to of order $10 \mu b$, with most measurements involving rather small numbers of events, typically on the order of a few thousand. The extant data from photoproduction are far too meager to perform the analysis necessary to unambiguously identify gluonic excitations. For example, after one year of low intensity running at 10^7 photons/sec, the yield of $a_2(1320)$ in GLUEX will be five orders of magnitude greater than the same collected in the SLAC photoproduction experiment. The yield of the exotic $\pi_1(1600)$ in the published E852 results will be increased by four orders of magnitude by GLUEX after one year of running.

There are reasonable sized data sets in 2π and 2π photoproduction from the CLAS detector at JLab that are currently under analysis. However, these arise from unpolarized photon beams and are produced from an incoherent bremsstrahlung spectrum that peaks at around 5 GeV .

0.A.6 Complementarity with other searches

Gluonic excitations include both exotic and non-exotic hybrid mesons and glueballs. Hybrid mesons exist in both the light quark (u , d and s) and heavy quark (c and b) sectors. Clearly, existing data collected with incident π beams, central collisions, $\bar{p}p$ annihilations and e^+e^- collisions have not uncovered a wealth of information about these states. As discussed earlier, the focus of the GLUEX project is in the light-quark hybrid sector. The initial benchmark states will be the exotic hybrids, which cannot mix with $q\bar{q}$ and therefore have a *smoking gun* signature. There are good reasons to expect that photoproduction will be particularly effective at uncovering the exotic hybrid mesons. And the existing photoproduction data are meager indeed.

The glueball and heavy hybrid sectors are not accessible to GLUEX. Glueballs are not preferentially produced in photoproduction because they do not couple to photons. Moreover, according to lattice QCD, the lightest exotic glueball has a mass of $4 \text{ GeV}/c^2$. One fruitful area of investigation are J/ψ radiative decays since the system recoiling from the photon should be rich in two-gluon states. The planned CLEO-c project at CESR will collect a billion J/ψ radiative decays.

The direct production of exotic hybrids in e^+e^- collisions is complicated by the fact that the angular momentum barrier (the excited flux-tube carries $J = 1$) suppresses this production mode.

Lattice QCD predictions about heavy-quark exotic hybrids are at least as reliable as for the light-quark hybrids but the experimental situation is far more problematic. The photoproduction cross-sections are a few orders of magnitude lower. At the higher energies needed to produce these more massive states many other uninteresting processes can contribute to background. Finally, to unambiguously tag a charm or beauty hybrid one must identify detached vertices, further complicating the experimental challenge.

0.A.7 Production and analysis of hybrid mesons

Kinematics

Consider a specific exclusive photoproduction reaction:

$$\gamma p \rightarrow X p \tag{1}$$

The center-of-mass energy squared, s , and the momentum-transfer-squared, t , between the incoming beam and outgoing X are defined in terms of the four-vectors of the particles:

$$s = (p_\gamma + p_p)^2 \quad (2)$$

$$t = (p_\gamma - p_X)^2 \quad (3)$$

The dependence of the cross section on s and t depend on the production mechanism, which is usually described in terms of the particle or particles which can be exchanged as shown in Figure 12. For example, if the exchange particle is the pomeron (diffractive process) the cross section is nearly constant in s . For meson-exchange processes, cross sections typically fall off with increasing s . The dependence on t is typically exponential:

$$\frac{dN}{dt} \propto e^{-\alpha|t|} \quad (4)$$

For the process (1) at high enough photon beam energy, E_γ , we can make the approximation $s \approx 2 \cdot E_\gamma$ where E_γ is in GeV and s is in GeV^2 . For fixed s and mass of X , m_X , there is a minimum value of $|t|$, or $|t|_{min}$, needed to produce X . This $|t|_{min}$ increases with increasing m_X for fixed E_γ and decreases with increasing E_γ for fixed m_X . Coupled with the steep dependence implied in equation (4), the dependence of $|t|_{min}$ on m_X will affect event yields. In addition, the line shape of a resonance can be distorted if there is too rapid a variation of $|t|_{min}$ across the width of a resonance.

Figure 13 shows an example of how the dependence in t is correlated with particle exchange. The distribution is in $|t'|$ where $t' = t - t_{min}$ for the D -waves after a PWA of the $\eta\pi^0$ system from the reaction $\pi^- p \rightarrow \eta\pi^0 n$ at $18 GeV/c$. The curves are fits to expected Regge exchanges for the various D -waves.

PWA requirements

The PWA technique is described in a later chapter. It is important to stress here that the detector design focuses on hermeticity and resolution to insure nearly uniform coverage with well-understood acceptance functions for various decay angles for particle X . Kinematic fitting will also be used to identify exclusive processes. The design focuses on the requirements of the PWA. The existence of well established resonances will be used as benchmarks for the PWA. They also provide benchmarks for the phase variation of

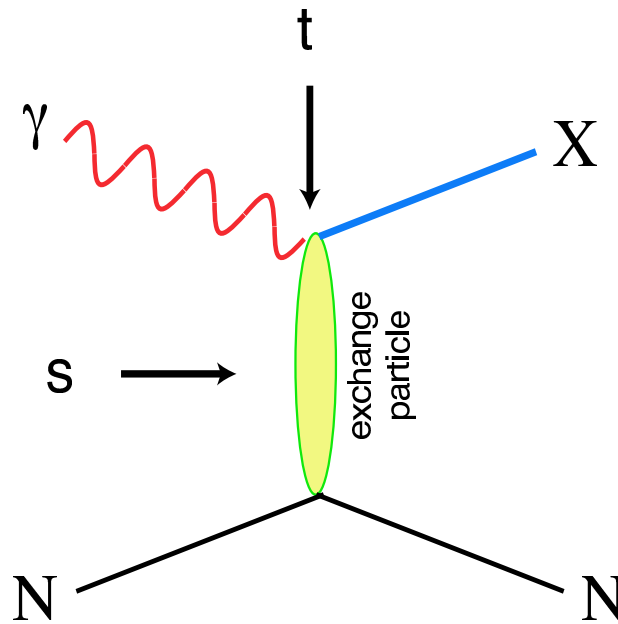


Figure 12: Diagram for the photoproduction of particle X . The variables s and t are the center-of-mass energy squared and the momentum-transfer-squared from incoming photon to outgoing particle X . The process shown here proceeds through the exchange of a particle in the t -channel.

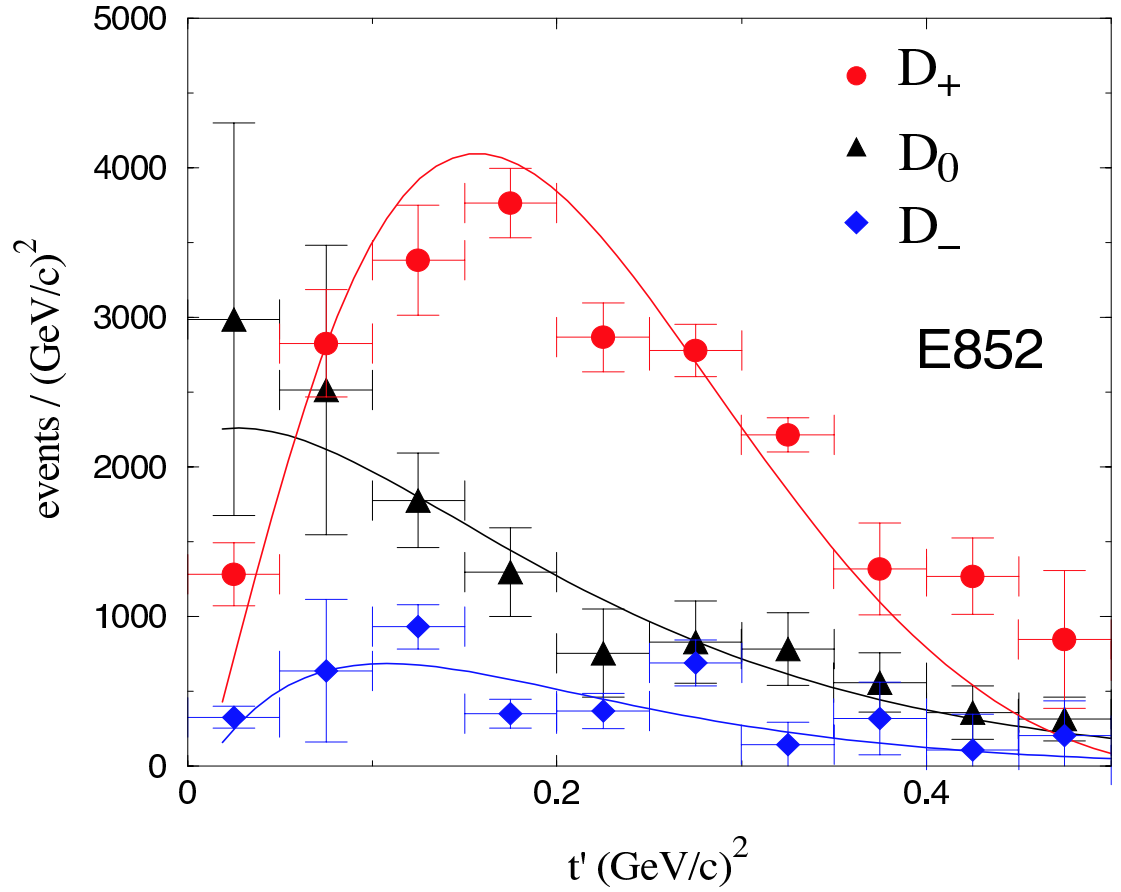


Figure 13: The distribution in $|t'|$ where $t' = t - t_{min}$ for the D -waves after a PWA of the $\eta\pi^0$ system from the reaction $\pi^-p \rightarrow \eta\pi^0n$ at $18 \text{ GeV}/c$. The curves are fits to expected Regge exchanges for the various D -waves.

candidate exotic states. Furthermore, candidate exotics can appear with multiple decay modes which must give consistent results. As an example, a meson which decays into $\eta\pi$ should be observed in channels where $\eta \rightarrow \pi^+\pi^-\pi^0$, $\eta \rightarrow 3\pi^0$, and $\eta \rightarrow 2\gamma$. Each of these modes leads to different acceptances and systematics. This provides a powerful check on PWA results.

Linear polarization of the beam

Linear and circular polarization

We start with a review of the relationship between linear and circular polarization. A right-handed-circularly ($|R\rangle$) polarized photon has $m = 1$ while for a $|L\rangle$ photon $m = -1$. These are related to the linear polarization states, $|x\rangle$ (in production plane) and $|y\rangle$ (perpendicular to production plane) by:

$$|x\rangle = \frac{1}{\sqrt{2}} (|L\rangle - |R\rangle) \quad (5)$$

$$|y\rangle = \frac{i}{\sqrt{2}} (|L\rangle + |R\rangle) \quad (6)$$

States of linear polarization are eigenstates of parity. We will use these relations in several straightforward cases to show how linear polarization:

1. can provide information on decays in lieu of statistics,
2. is essential in isolating production mechanisms, and
3. can be used as an exotics filter if the production mechanism is known.

Linear polarization and statistics

To illustrate how linear polarization provides useful information in the PWA, consider the case of the photoproduction of a vector meson which subsequently decays into two pseudoscalar mesons. Possible examples are $\rho \rightarrow \pi\pi$ or $\phi \rightarrow K\bar{K}$. Suppose the production mechanism produces the vector with the same helicity as the incident photon (or *s-channel*

helicity conservation). In the rest frame of the vector the two-pseudoscalar wave function is described by

$$Y_1^m(\theta, \phi) \propto \sin \theta \cdot e^{im\phi} \quad (7)$$

For circularly polarized photons (either $m = 1$ or $m = -1$) the square of this amplitude carries no ϕ information while for in-plane photons there is a $\cos^2 \phi$ dependence and out-of-plane a $\sin^2 \phi$ dependence in the decay angular distribution, since in these cases we have the sum or difference of Y_1^{+1} and Y_1^{-1} according to equations (5) and (6). Although not essential in determining spin, a gain of statistics is needed to recover a drop in the degree of linear polarization. For example, our Monte Carlo simulation studies indicate that when the degree of linear polarization decreases from 0.40 to 0.2 a factor of two increase in statistics is needed to achieve the same relative error in determination of spin amplitudes.

Linear polarization and production mechanism

This is best illustrated by considering a specific example. Suppose we produce a vector particle ($J^P = 1^-$) by the exchange of a scalar particle ($J^P = 0^+$ – natural parity exchange) or a pseudoscalar particle ($J^P = 0^-$ – unnatural parity exchange). We wish to determine whether the vector is produced by natural (amplitude A_N) or unnatural (amplitude A_U) parity exchange. In the center-of-mass of the vector particle, the momentum vectors of the beam photon and exchange particle are collinear. For circularly polarized photons, the m of the vector is the same as that of the photon. From parity conservation, the orbital angular momentum between the photon and exchange particle is $L = 0$ or $L = 2$ for natural parity exchange and $L = 1$ for unnatural parity exchange. So for circularly polarized photons, with $m = +1$, the total amplitude is $A_N + A_U$ whereas for $m = -1$, the total amplitude is $A_N - A_U$. This follows simply from the addition of angular momenta. Circularly polarized photons allow us to measure only the sum or difference of the two exchange amplitudes. If however, we have linearly polarized photons along the x -direction, we extract A_N using equation (5) and for polarization along the y -direction, we extract A_U using equation (6).

Linear polarization as an exotics filter

Using arguments similar to those above, it has been shown [Af00] that linear polarization can be used as a tool to filter exotics. For example, a $\rho\pi$ system with $I = 1$ has $C = +$. Suppose that one can determine the naturality of the exchange particle by selecting data within a range of $|t|$. For a produced $C = +$ particle with spin one we can have natural parity ($J^{PC} = 1^{-+}$ – exotic) or unnatural parity ($J^{PC} = 1^{++}$ – non-exotic). In the case of natural parity exchange the in-plane polarization selects the $J^{PC} = 1^{-+}$ wave while

out-of-plane polarization selects $J^{PC} = 1^{++}$. For unnatural parity exchange the reverse is true. Note that in this case, we are specifying the naturality of the exchange and using linear polarization to select the naturality of the produced particle. In the previous section, we specified the naturality of the produced particle and used linear polarization to select the naturality of the exchanged particle.

0.B The GlueX Experiment in Hall D

0.B.1 Introduction

The goal of the GLUEX experiment is to search for gluonic excitations of $q\bar{q}$ pairs with masses up to $2.5\text{ GeV}/c^2$. The identification of such states requires knowledge of their production mechanism, identification of their quantum numbers, J^{PC} , and measurement of their decay modes. These in turn require a partial wave analysis of exclusive final states. The decay products of produced mesons must be identified and measured with good resolution and with full acceptance in decay angles. In many cases, the decays of mesons involve a chain of particle decays. The GLUEX detector must therefore be hermetic (effective 4π coverage) and have the capability of measuring directions and energies of neutral particles (γ , π^0 , η) and four-momenta of charged particles with good resolution. Clearly, particle identification is also required.

The partial wave analysis technique depends on high statistics and, in the case of incident photons, also requires linear polarization. The latter is needed to identify the production mechanism. The linear polarization is achieved by the coherent bremsstrahlung technique. The degree of linear polarization and flux of photons in the coherent peak fall dramatically as the photon energy approaches the endpoint energy. On the other hand, it is desirable to have photon energies high enough to produce the required masses with sufficient cross-section and with sufficient forward-boost for good acceptance. For a fixed incident momentum and a fixed resonance mass, it is also desirable to have a fairly constant $|t|_{min}$ over the natural width of the resonance. This requirement demands a higher incident photon energy than expected by simple threshold production.

An operating photon energy of 9.0 GeV produced from a 12.0 GeV electron beam represents an optimization of beam flux, cross-section and degree of polarization. The GLUEX detector is optimized for this energy range. Extensive Monte Carlo simulations has been performed to optimize the detector's ability to reconstruct exclusive final states. Acceptances are nearly 90% for many complicated channels, and the detector resolutions have been balanced to facilitate excellent reconstruction of the events. This will allow kinematic fitting to reduce background contamination of events. Such backgrounds are known complications in partial wave analysis.

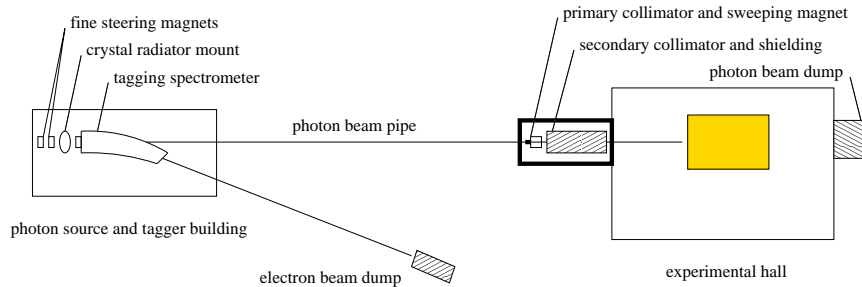


Figure 14: A schematic plan view of HALL D photon beam line for the GLUEX experiment, (shown in the horizontal plane as viewed from above). The objects in this figure are not drawn to scale.

0.B.2 The Photon Beam and Polarization

Linearly polarized photons can be produced in the desired energy range by using the technique of coherent bremsstrahlung. A horizontal plan view of the photon beam line is shown in Fig. 14 with the major components labeled. The electron beam enters the figure from below ground at the left and is bent into the horizontal plane to enter the tagger building. There it passes through two small dipoles to impinge upon the bremsstrahlung radiator.

The Photon Tagger and Beam Collimation

After its exit from the radiator, the electron beam passes into the tagger magnet where the primary beam is bent in the direction of the electron beam dump. The radiator crystal is thin enough that most of the electrons lose less energy in traversing the radiator than the intrinsic energy spread of the incident beam. Those electrons which lose a significant fraction of their initial energy inside the radiator do so by emitting a single bremsstrahlung photon. These degraded electrons are bent out of the primary beam inside the tagger magnet and exit the vacuum through a thin window, passing through air for a short distance to strike the focal plane of the spectrometer. The primary electron beam is contained inside vacuum all the way to the dump.

The tagging system used in the GLUEX experiment will consist of a dipole magnet spectrometer with two sets of plastic scintillation counters in the focal plane to tag photon energies: a precision set with 0.1% energy resolution and a broad-band set with a coarser energy resolution of 0.5%. The precision system will be composed of 64 narrow counters and will nominally tag photons from 70% to 75% of the electron beam, but will be movable allowing precision tagging of other energy bytes as well. The broad-band tagging system

will tag photons between 25% and 92% of the electron beam energy using 128 fixed scintillation counters. The second system will be crucial for alignment of the radiator crystal and could also be used by other experiments that might be run in HALL D.

The tagger magnet will be similar to the existing tagger in Hall B of Jefferson Lab. The higher energy needed in GLUEX is largely compensated for by going to smaller bend angles, so the sizes of the magnets are comparable, although the HALL D system will bend in the horizontal rather than in the vertical plane.

The photons that are produced in the radiator pass through a small hole bored in the return yoke of the tagger magnet and exit the vacuum through a thin window in the forward direction. They then pass into a transfer pipe, which may either be evacuated or filled with helium to reduce photon beam degradation due to interactions, and travel to the experimental hall. Just before entering the hall the photon beam passes through a system of collimators and sweeping magnets. In the Fig. 14 they are shown in a separate enclosure for shielding purposes. The primary collimator is first. It selects the part of the photon beam that is allowed to reach the target. Debris from interactions along the inside surface of the collimator bore forms a halo around the photon beam that exits the collimator. The charged component of the halo is deflected away from the beam axis by a dipole “sweeping” magnet just downstream of the collimator. A secondary collimator follows the sweeping magnet to stop the deflected shower particles and block the halo of secondary photons generated by the first collimator. This collimator is of a larger diameter than the primary and so sees a reduced rate of secondary interactions on the inner surface of the hole. Any new showers that are generated there are cleaned up by a second sweeping magnet. The beam then passes through a final collimating aperture into the experimental hall. This triple-collimation system was copied from the setup developed at SLAC [Ka75].

The collimated photon beam, now only a few mm in diameter, is delivered to the experimental target. After traversing the target (3% radiation lengths), the photon beam passes through the detector and into the photon beam dump at the back of the HALL D building. Based upon a design upper limit of 60 kW (5 μ A at 12 GeV) being delivered to the electron beam dump, the total power in the photon beam is at most 1.5 W in the experimental hall and at most 15 W in the collimator enclosure. The safety issues of such a beam have been reviewed by Jefferson Lab’s RadCon group. As an additional safety constraint, permanent magnets will be installed in the photon beam down stream from the tagger building to prevent an accidental loss of the electron beam into HALL D. These magnets have been obtained as surplus from FermiLab.

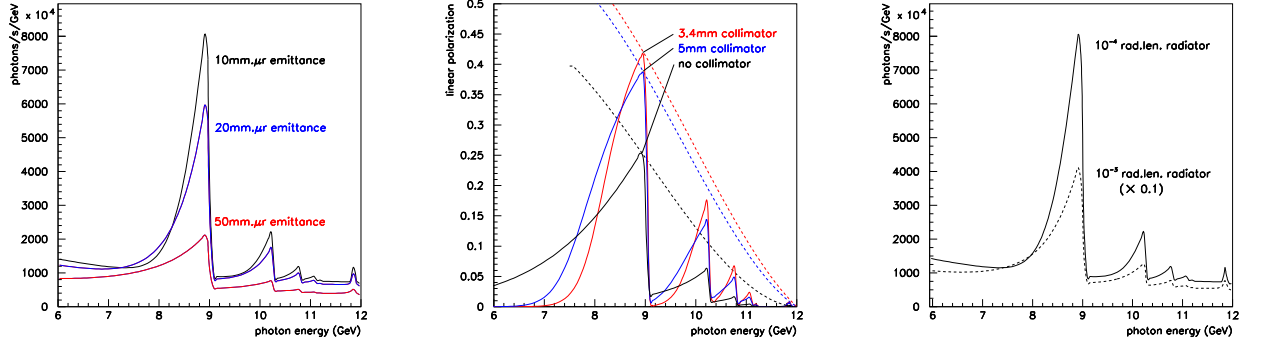


Figure 15: Left: The effect of collimation on the coherent bremsstrahlung spectrum, (various collimation diameters are given with the optimum value being 3.4 mm). Center: Plane polarization of the coherent bremsstrahlung. The dashed lines indicate the trajectory of the peak polarization. Right: Collimated coherent bremsstrahlung spectrum for 2 crystal radiator thicknesses.

Polarization via Coherent Bremsstrahlung

The net polarization of the beam under different collimation conditions is shown in Fig. 15 (center panel). The dashed curves show how the maximum polarization in the peak varies as the peak energy is changed by rotating the crystal. The polarization in all cases is zero at the endpoint, but its dependence on the electron beam energy E and photon energy k is different. Without collimation it rises as $(k - E)^2$, one power coming from the intensity of the coherent peak relative to the incoherent component and goes linearly to zero at the endpoint, and the other from the intrinsic polarization of the coherent photons that also behave like $(k - E)$ near the endpoint. Collimation allows one to essentially isolate the coherent component, so that the polarization available to the experiment rises from zero at the endpoint in a linear fashion. The dashed curves in Fig. 15 demonstrate this point.

In order to obtain the full polarization enhancement from collimation, it is necessary to have a distance between the radiator and collimator of about 80 m. This distance scale is set by the requirement that the collimator aperture must be large compared to the size of the electron beam spot on the collimator, but small compared to the actual photon spot size. Fig. 15 shows the maximum polarization as a function of radiator-collimator distance for a coherent peak at 9 GeV. The collimator diameter is adjusted in this calculation to keep the collimation half-angle at $0.5 m_e/E$. At zero distance the collimator has no effect except to attenuate the beam, and so the uncollimated polarization from coherent bremsstrahlung is obtained. At 100 m separation distance the polarization enhancement

has saturated. The design for HALL D calls for a radiator-collimator distance of 80 *m* with a collimator diameter is 3.4 *mm*.

The range of permissible thicknesses for a crystal radiator is bounded from above by multiple scattering of the electron beam as it passes through the radiator, which causes the divergence of the incident beam to grow, thereby enlarging the photon beam spot on the collimator face and degrading the degree to which collimation discriminates against the incoherent component in favor of the coherent part. It is bounded from below by the fact that the crystal must be of some minimum thickness in order to achieve the full coherent gain. For a 12 GeV beam energy and a 6 GeV coherent photon the coherence length is 18 nm. The coherence length does not impose a practical limit on how thin the radiator should be. The effects of multiple scattering are best presented by showing the calculated spectra for various radiator thicknesses. The photon spectrum for a 20 μm (10^{-4}) and a 100 μm (10^{-3}) radiator is shown in Fig. 15 to demonstrate the effect. The 100 μm spectrum is scaled down by a factor of 5 to facilitate the comparison, but it is clear that for a significant coherent gain, the crystal thickness must be near 20 μm .

Synthetic diamonds are made using either vapor deposition (CVD) or high pressure high temperature (HPHT) techniques. CVD diamonds have an extensive mosaic and are unsuitable for coherent bremsstrahlung. However HPHT synthetics look very promising, and the Glasgow group have recently acquired a 5 *mm* \times 5 *mm* synthetic diamond less than 18 μm thick which has a [100] orientation. This diamond yielded a very good coherent bremsstrahlung spectrum and X-ray measurements showed rocking curve widths of less than 10 μr , quite close to the ideal value for diamond.

A 30-*cm*-long liquid hydrogen target will be used. It will be contained in the same vacuum jacket as the photon tagger radiator and will be constructed of low mass materials. The collimated photon beam will be contained within a radius of 2.5 *cm* from the beam axis. This will allow adequate space between the hydrogen vessel and the innermost detector element for insulation, a vacuum pipe and any plumbing and wiring required to instrument the target.

0.B.3 The GlueX Detector

The GLUEX detector has been optimized to provide nearly hermetic acceptance for both charged particles and photons. In addition, a combination of particle identification systems will allow very good K - π separation. Design optimization will allow the detector to fully reconstruct exclusive many-body final states. In conjunction with high statistics, this will allow excellent partial wave analysis of many final states. Fig. 16 is a schematic

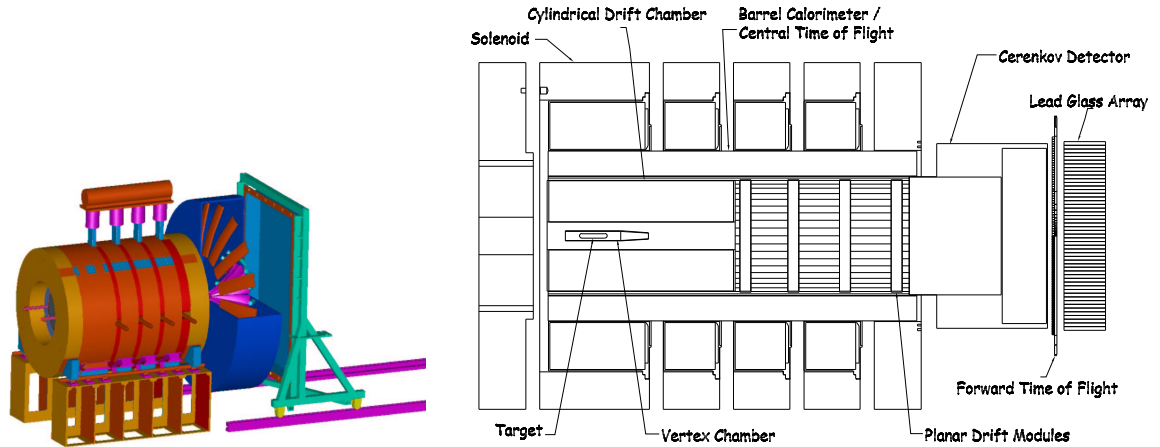


Figure 16: A 3D cutaway view of the GLUEX detector (left) and schematic diagram of its major subsystems (right)

representation of the proposed detector with the individual subsystems discussed briefly below. A more detailed description can be found in the GLUEX Design Report [GX02].

The Super-conducting Solenoid

Momentum analysis in GLUEX will be provided by a nominal 2 Tesla superconducting solenoid magnet. This solenoid was built at SLAC ca. 1970 for the LASS spectrometer [As87] and subsequently moved to LAMPF in 1985 for inclusion in the MEGA spectrometer. The MEGA Experiment and the solenoid were decommissioned in place in 1995. The MEGA experiment has since been removed from the solenoid and arrangements are underway to ship the solenoid from LANL to the Indiana University Cyclotron Facility (IUCF) for refurbishment and testing. This magnet was designed and built using standards that today would be considered ultra-conservative. The magnet employs a cryostatically stable design and uses cryostats that were designed to be easily opened for service with hand tools. A recent inspection of the magnet at LANL revealed that it is still in excellent condition and worthy of the time and cost involved in relocation and refurbishment. Nevertheless, the magnet support systems are now 30 years out of date so even though the magnet is in excellent condition it requires some maintenance, updating, and modifications for use as part of the GLUEX experiment.

The LASS/MEGA solenoid was inspected in April 2000 by a team from the GLUEX collaboration, JLab staff and two of the original designers of the magnet. This team met at Los Alamos with the MEGA staff and inspected the magnet installation and the fourth coil. Except for two small mechanical vacuum pumps the system was completely intact.

The committee concluded that “the condition of the magnet is excellent and if cooled down in place would in all likelihood work!” Subsequently, Jefferson Lab formally transferred the solenoid system from Los Alamos to JLab as of October 2001. A Memorandum of Understanding (MOU) was negotiated with LANL to cover all disassembly aspects of the MEGA experiment. This work, performed by a JLab crew, began in November 2001 and was completed in February 2002. The solenoid is now bare and awaiting final disassembly and shipment to IUCF. An MOU was negotiated between JLab and IUCF to receive the solenoid, perform all the upgrade and maintenance work, and perform a full scale cryogenic system test of the solenoid. A detailed description of the work needed to bring the magnet systems up to date and have the magnet operational in the GLUEX experiment can be found in reference [GX02].

Particle Tracking and Particle Identification

The system of tracking chambers in the GLUEX detector must cover as close to a 4π solid angle as possible over a wide range of particle momenta, and have sufficient momentum resolution to be able to identify missing particles. In the solenoid region, the chambers are inside the barrel calorimeter. The location of the target, very near the entrance to the solenoid, coupled with the energies involved which force the reaction products into forward angles, result in an effective 4π coverage in the center-of-mass of the produced particles, even though the geometrical coverage around the target is less than that. The chambers also must extend as close to the beam line as possible. Near the target, this will provide very accurate vertex information which will be important in identifying decaying particles (e.g. K_S , Λ , Σ , ...). In the forward region, this is needed to reconstruct very fast particles ejected at small angles (down to nearly 0°). Finally, at large angles, the tracking must be able to separate π 's and K 's up to momenta of about $0.5 \text{ GeV}/c$ — a regime where dE/dx measurements will work. To satisfy the tracking requirements, a starting point based on the LASS detector [As87] was used. A series of three different tracking elements will be implemented, with each element optimized for a particular region in the detector as shown in Fig. 16.

The Vertex Detector

The Vertex System (VTX) surrounds the target and has several purposes. First it will be used to provide accurate tracking information very close to the target. These track elements must be sufficiently well defined to be connected to the other tracking chambers. Secondly, the VTX must provide a fast signal (start signal for the event) which can be used in the level -1 trigger of the experiment. Finally, it is a critical element of all time-of-flight systems. The vertex detector will consist of two detector packages. One will be optimized for timing purposes and the other one will provide fast tracking information (see Fig. 17).

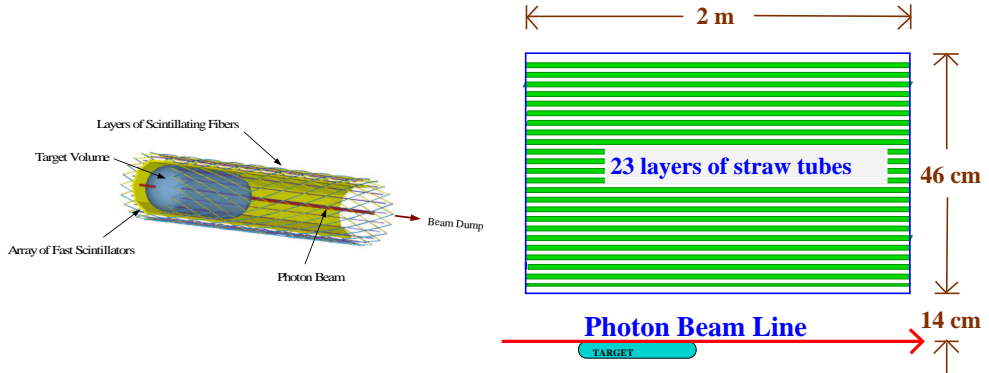


Figure 17: Left: The start counter/vertex chamber. Right: The straw tube chamber.

The timing detector will consist of a cylindrical array of 10 scintillator paddles. This will allow us to cover scattering angles between 1° and 90° for the full length of the target. The scintillators have a thickness of 5 mm which reduces to 2 mm in the forward direction. This will provide good light output and therefore a good timing signal. Using Bicron BC-404 scintillating material in combination with fast photo multipliers should result in an overall timing resolution better than 120 ps.

The fast tracking detector will consist of three super-layers of fibers, each containing two layers to minimize dead space. The central layer will be arranged around the target and parallel to the beam, and will determine the azimuthal angle. The z position is deduced from the two outer layers. They will be wound in two opposite helices around the first layer. In order to function in the high magnetic field, we are studying the possibility using Visible Light Photon Counters (VLPC) developed by Rockwell in collaboration with Fermilab [Pe89]. The spectral sensitivity of the VLPCs require us to use SCSF-3HF multi clad scintillating fibers from Kuraray which have a long attenuation length of 5.5 m and are also the least susceptible to radiation damage. One of the main advantages of using VLPCs is their large quantum efficiency of approximately 80% [Wa97] for the light produced by the fibers together with a very high rate capability of 10^8 single photoelectrons per second. The design of this detector system will closely follow the prototype system developed by the D0 collaboration at FNAL [Ba96]. The expected position resolution will be less than 1 mm.

The Cylindrical Drift Chamber

The Cylindrical Drift Chamber (CDC) surrounds the VTX and provides very good $r - \phi$ information and moderate-to-good z information. This chamber also provides dE/dx information for tracks which do not reach any time-of-flight detectors. The CDC is used to

accurately track particles between polar angles of 20° and 170° . To minimize material in the forward end plate of the chamber, the chamber must be self-supporting. This leads to a straw chamber, where the straw walls support much of the wire tension. The disadvantage of this design is the difficulty of making dE/dx measurements in a circular straw tube, which requires careful primary path-length corrections.

The straw-tube chamber will contain 3349 straws, each of which is 1.6 cm in diameter. They are arranged in 23 layers. Eight of the 23 layers will be stereo tilted by $\pm 6^\circ$ from the straight tubes. Fig. 17 schematically shows the arrangement of the tubes in the chamber. The tubes are assumed to have an $r - \phi$ resolution of $200\ \mu\text{m}$, while resolution along the wire length will be obtained using the stereo layers. This will nominally yield a resolution along the length of the wire of about $200\ \mu\text{m}/\sin(6^\circ)$ or about 1 mm . The chamber end plates are 0.95 cm thick, and constructed as eight separate *pie-shaped* pieces. The chamber plates extend between an inside radius of 14 cm and an outer radius of 60 cm . Current plans call for no inner shell, and an 8 mm thick outer fiberglass shell. The straw tubes consist of $100\ \mu\text{m}$ thick aluminized kapton, and have $20\ \mu\text{m}$ diameter gold-plated tungsten wires in them. In order to study the behavior of straw tube chambers, a 2 m long chamber with 2 cm diameter tubes has been acquired from the EVA experiment at Brookhaven.

In the construction of the straw-tube chamber, the most technically difficult to construct are the stereo tubes. A 1/3-scale model of the chamber has been built with the specific purpose of understanding the construction difficulties of the stereo layers, and has demonstrated the importance is the transition region from straight to stereo layers. A prototype of the end plate is currently being built to determine how accurately the plate can be built.

The choice of gas also plays a significant role in the chamber's performance due to the 2.25 T magnetic field in the detector. In order to study this, the GARFIELD program [Ga84] has been used to compute electrostatic properties of the straw tubes, both with and without the magnetic field. The chamber will require a *slow* gas in order to minimize the *Lorentz angle*. Calculations indicate that the maximum drift time will be on the order of 500 ns in such a mixture. Investigations are currently underway with mixtures containing larger fractions of CO_2 , a slow gas known to work well in high magnetic fields.

The Forward Drift Chambers

The Forward Drift Chambers (FDC) are disk-shaped drift chambers. The basic drift package is a plane of wires with $150\ \mu\text{m}$ spatial resolution between two planes of cathode strips. The strips are arranged in a u and v geometry with respect to the wires, allowing the reconstruction of a 3-D space point from each hit. The chambers are arranged in

packages of six, which results in a small track segment, so as to facilitate a later linking of the tracks. Given the number of spiraling tracks, it is critical that these chamber packages not only provide good spatial resolution, but also reasonable directional information. The basic chamber element is a disk with an outer radius of 60.0 *cm* and the wires strung as chords across the chamber. With a 1.0 *cm* wire spacing, each chamber will contain 119 wires. In addition, there will be an equal number of cathode strips on each face. These are arranged in a *u-v* pattern with respect to the wires. The wires that cross through the beam line will be deadened out to a radius of about 3.5 *cm* by placing material such as Styrofoam in the chambers.

Monte Carlo studies show that the combined tracking system provides very good momentum resolution for the event topologies in GLUEX. The system is sufficient to identify undetected particles by missing mass cuts. In particular, a missing neutron can be separated from a completely missing recoil Δ for most kinematic regions. Detailed information on resolutions can be found in reference [GX02].

Electromagnetic Calorimetry

The goal of the GLUEX calorimetry is to detect and measure photons from the decays of π^0 's and η 's, which, in turn, can come from the decays of produced mesons, or from an excited baryon (N^* or Δ). The positions and energies of the photons must be of sufficient accuracy to allow for a complete kinematic reconstruction of the event. Finally, for events with only charged particles, it is essential to be able to veto on neutral missing energy. Thus, nearly hermetic coverage is critical. For selected triggers, neutral energy requirements (or vetoes) are relatively easy to implement.

Calorimetry in the GLUEX experiment will be handled by three different detector systems. In the forward region ($\theta > 14^\circ$), a circular array of lead-glass (Pb-Glass) crystals will be used. In the central region ($14^\circ < \theta < 138^\circ$), a lead-scintillating-fiber matrix calorimeter will be deployed, and in the backward region ($\theta > 138^\circ$) an iron-scintillator photon veto detector will be the likely choice. In the forward and central region, it is necessary to be able to accurately reconstruct the photon energy and direction for physics event, whereas, photons in the backward direction can only result from background events and only a veto system is necessary.

The Forward Calorimeter

The Forward Calorimeter in the GLUEX experiment is a circular lead glass array (see Fig. 18). The crystals have been salvaged from an existing detector, the Brookhaven National Laboratory E852 lead glass calorimeter [Cr98], and are currently in storage at

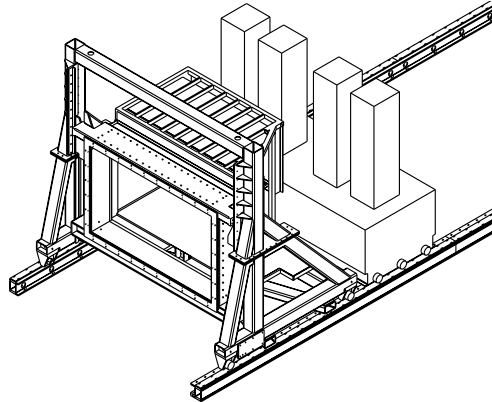


Figure 18: A sketch of the Pb–glass array as modified for the GLUEX detector. The glass is stacked in a circular arrangement to match the solenoid.

JLab. In order to be used in the GLUEX experiment, a new support structure will need to be constructed. This will allow the crystals to be stacked in a circular arrangement and the detector package to move in and out of the GLUEX detector region. Moreover, new Cockcroft-Walton base similar to those used in the JLab Rad ϕ experiment will be used. Finally, the gated ADCs used in E852 will be replaced with 8 bit, 250 MHz FADCs to eliminate dead time and allow digital pipeline triggers.

The calorimeter has a measured resolution, σ_E/E in percent which can be parameterized as $a + b/\sqrt{E [GeV]}$ where $a = 1$ to 2 and $b = 5$. The average spatial resolution is 2 to 4 mm and decays with up to eight photons are routinely reconstructed.

Operating an electromagnetic calorimeter, like the LGD, near a high-intensity (a few $\times 10^7$ photons per second) photon beam line could be a concern given the backgrounds one might expect with a tagged bremsstrahlung photon beam. For this reason, the experience with the LGD used in the Radphi experiment in the Hall B photon beam is of particular relevance. Because of the high quality of the photon beam, beam-associated backgrounds were manageable, even when operating at an endpoint energy of 4 GeV. At higher energies the beam spot size will be even smaller and the LGD energy resolution will improve.

The Barrel Calorimeter

The Barrel Calorimeter, shown schematically in Fig. 19, will utilize scintillating fibers embedded in a lead matrix to make a relatively high–resolution sampling calorimeter. Advantages include speed, cost, ease of readout, and the fact that it is based on a proven technology. This technology has been used in calorimeter design and operation for more

than a decade. The ratio of the active scintillator to the passive high- Z material, as well as the diameter of the fibers can be tuned to enhance resolution, to determine the radiation length, and to achieve uniformity in the electromagnetic to hadronic response (the e/h ratio). For high-resolution EM performance, the JetSet detector developed at Illinois [He90] was the first designed specifically to optimize EM resolution. The recipe produced a detector comparable to lead glass at a considerably lower cost and with approximately half the radiation length. Our design for GLUEX follows this concept but would be a full 12.5-15 X_0 thick at normal incidence and considerably longer. Realization of these changes fortunately can be based on the KLOE calorimeter at DAΦNE, a device of the same length as the barrel calorimeter but with an even larger inner diameter [An96]. The KLOE detector has achieved an excellent energy resolution parameterization of $\sigma/E \approx 4.4\%/\sqrt{E}$ in a half-length prototype, using 1 mm -diameter scintillating fibers, and 0.5 mm -thick lead sheets.

For GLUEX, we will build 54 modules each 4.5 m in length and 20–25 cm deep, using the same diameter of fibers and thickness of lead sheets as for the KLOE detector, (see Fig. 19). The readout scheme takes advantage of the fact that all fibers run parallel to the axis of symmetry of the solenoid and therefore all light piped to the ends of the modules retains its azimuthal and radial information. Since this device is located near the central region of the solenoid, where the magnetic field is around 2 Tesla, field-resistant readout must be employed. The most promising candidate seems to be hybrid photo diode devices that have been developed for CERN applications. These devices have a very fast rise time of 6 ns or less, a fast fall time of less than 10 ns, and excellent energy resolution. They are immune to magnetic fields up to 2 T and their power supplies are very compact due to the fact that they draw virtually no current even under maximum bias. The polished ends of the lead, scintillating fiber matrix will be coupled to multiple independent light guides or to a fiber-to-fiber mask.

An important feature of these detectors is the signal rise-time and overall duration. Because fast plastic scintillator is used, integrated signal time can be kept below 100 ns with shorter times possible if deemed necessary for rate considerations. At the expected maximum luminosity no problems are anticipated. With short rise-times, very good timing can be expected for each of the PMTs involved in collecting the light from a shower. Time differences from the two ends produces the z coordinate of the hit. The mean light collection time of the two readout ends can be used to determine the particle time-of-flight (TOF). TOF coupled with the track length and momentum then yields particle mass. In the KLOE design, timing of ≈ 250 ps (RMS) was achieved, and improvements are possible.

In order to construct 4.5 m long modules, we have been studying the KLOE tooling development. Several visits of HALL D physicists to Frascati and Pisa have already taken

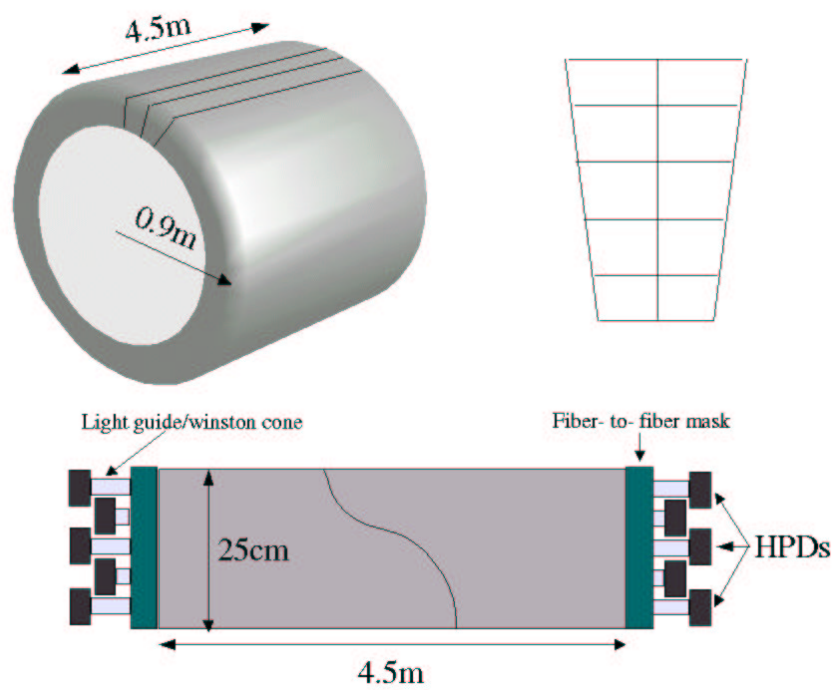


Figure 19: Sketch of the Barrel Calorimeter made from bars of Pb/SciFi material. Upper left: perspective view; upper right: close up of end with suggested readout segmentation for one of the 54 bars; Lower: side view showing approximate locations of the PMTs.

place and their training in the use of the KLOE 15 *cm*-wide lead swagging machine is nearly complete. In May 2002, we successfully swagged 0.5 *mm* thick lead sheets, and glued 10 layers of lead and 1 *mm* optical fibers together, producing the first Pb/SciFi test module with dimensions 100 *cm* x 15 *cm* x 1.25 *cm*. This swagging machine is now located at Regina on loan from Frascati, where the construction of larger modules is well under way.

We have conducted several static tests at Regina and in-beam tests at TRIUMF of several makes of single- and multi-clad SciFi strands have also been conducted, from Kuraray and Pol.Hi.Tech. The main features of the results were in close agreement with benchmark tests from KLOE. The Kuraray fibers showed a consistently superior performance as per the light attenuation coefficient. They also exhibited a better timing resolution. However, the Pol.Hi.Tech. multi-clad fibers performed better in terms of light yield, based simply on the observation that for the same bias and gain the mean of the ADC spectra for these fibers was higher. For this reason, multi-clad fibers have been ordered from Kuraray and their testing is in progress.

Finally, considerable R&D has gone into the investigation of the performance of the hybrid PMTs as well as toward the development of a suitable pre-amplifier electronic circuit. In our tests we used the DEP PP0350G hybrid PMT and its PP0100Z HV power supply. This device is powered by a HV supply which is typically set to -8 to -9 kV, and a bias of -60 to -80 V is applied across the diode. The gain response of the hybrid PMT at -8 kV is around 1600, which necessitates the use of a preamplifier. For our initial evaluation, we have used a Cremat¹ CR-101D charge sensitive pre-amplifier. Its rise time is 13 ns, its input capacitance is 20 pF and its power dissipation is 150 mW. These tests have pointed to the great care which must be exercised so as to electrically isolate the circuits. Much effort was expended in the avoidance of current (ground) loops in the circuit and in the shielding of the circuits from RF noise. Many parameters of the circuit were studied, such as rise time, signal amplitude, ADC response and photo-cathode positional sensitivity. All measurements were very promising and we are confident that we are close to a production design.

The Upstream Photon Veto

The Upstream Photon Veto is needed to be able to detect and veto on photons traveling in the backward direction. Detailed Monte Carlo studies have shown that events in which a baryon resonance is recoiling against the meson system can produce photons, from the baryon decay, which are traveling in the backward direction. The detector is a soft-steel scintillator sandwich device located directly upstream of the target and in place of the solenoid's original field shaping mirror plate. In the current design, the mirror plate is

¹Cremat Inc., 45 Union Street, Watertown, MA 02472, USA.

modified by removing all of the soft iron within the inner solenoid radius. This modification effectively removes the upstream mirror plate leaving only a soft iron annulus the size of the magnet coils and has several benefits: it allows the addition of an upstream photon veto, and upstream access to the target region, cylindrical drift chamber, and the upstream end of the barrel calorimeter.

The photon veto consists of 18 layers of 1 *cm* thick scintillator alternating with first 12 layers 0.635 *cm* ($0.36X_0$) thick steel sheets then 6 layers of 1.270 *cm* ($0.72X_0$) thick steel sheets (see Fig. 20). Each scintillator layer consists of seven $34\text{ cm} \times 238\text{ cm}$ paddles forming a plane. The central paddle has a hole to allow for the passage of the beam and the target support and cryogenic system. The effective area of each plane is approximately $238\text{ cm} \times 238\text{ cm}$. The total counter thickness is 33.25 *cm* ($8.91X_0$). The layers are arranged into three alternating orientations: *x*, *u*, and *v* (± 45 deg, respectively).

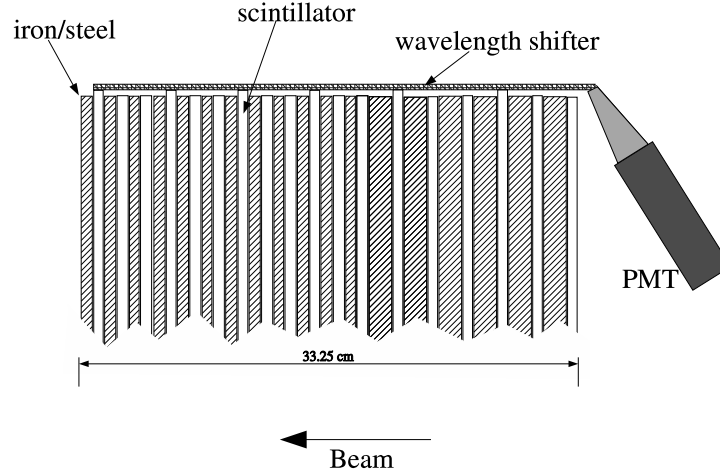


Figure 20: Sketch of a upstream photon veto segment. The 18 scintillator layers are arranged into three alternating orientations: *x*, *u*, and *v*. Shown is the light collection for one such orientation. The light collecting ends of the scintillators are joined together via a wavelength shifter which is oriented perpendicular to the scintillators. The wavelength shifter is used to redirect the light through 90° and out the upstream end of the solenoid to photomultiplier tubes (PMT).

Charged Particle Identification

Charged particle identification (PID) separates π^\pm from K^\pm from p (and the occasional \bar{p}). (We do not consider e^\pm nor μ^\pm identification explicitly, but they can be separated from hadrons at some level using the electromagnetic calorimeters.) Two detector systems

will be constructed explicitly for this purpose, namely the time-of-flight hodoscope and the Čerenkov detector. Both of these address PID in the forward region, where velocities are close to c and the separation is the most difficult. In the solenoid, we expect to make use of dE/dx in the drift chambers and timing in the barrel calorimeter. Furthermore, constrained fitting is a generally useful tool for identifying the event topology as a whole.

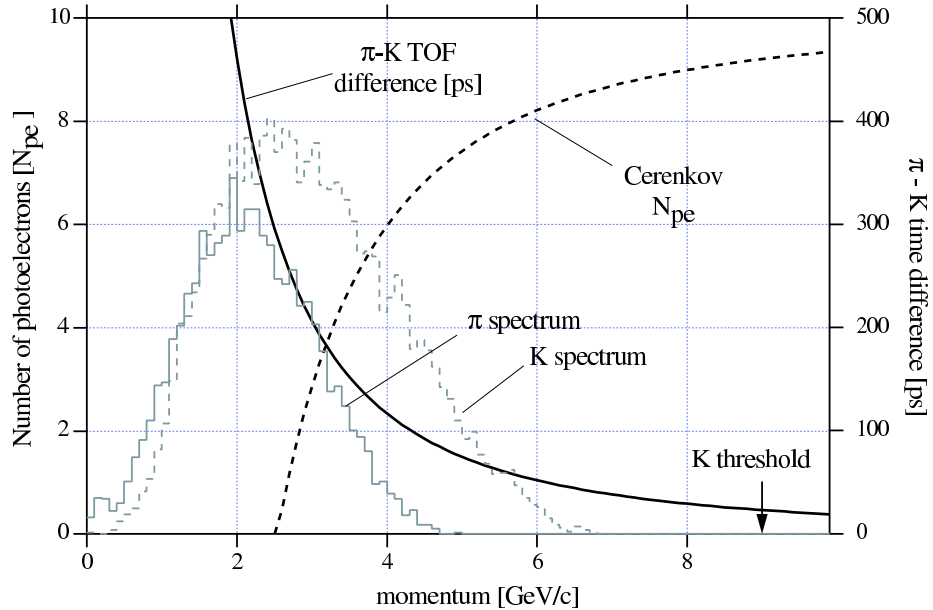


Figure 21: The time of flight difference between π and K mesons and the number of photoelectrons from the Čerenkov counter as a function of momentum. Also shown are expected π and K momentum spectra for $K^*\bar{K}^*$ final states.

If the particle momentum is not too high, time-of-flight is useful for PID in the forward region. For TOF scintillators that are 2 m long, RMS time resolutions on the order of 100-200 ps are typically achievable using well established techniques [Mo79, Be82]. With improvements in photomultiplier design, however, one can achieve 50 ps RMS for detectors with long, narrow geometry. Superior time resolution has also been achieved with mesh PMTs which will work well in a high magnetic field. In Fig. 21 shows range of relevant momenta for particle identification for both the time-of-flight system and the Čerenkov counter. Beam tests of prototype time-of-flight designs have been carried out and the results indicate we are well on track to achieving time resolutions below 100 ps.

The Time-of-Flight System

In the forward region the TOF system will consist of two walls of scintillation counters

oriented perpendicular to each other and located downstream of the Čerenkov counter and just upstream of the lead glass detector (LGD). The scintillator bars need to be 2 *m* long to cover the active regions of the Čerenkov counter and LGD. The bars will be read out at both ends with photomultipliers. The width of the bars is set by the requirement that the overlap of charged particles from the same event at the TOF in any one bar be acceptably small ($< 2\%$).

Extensive prototype studies have been carried out to optimize the TOF system design [De01]. Data using scintillation bars of various dimensions and manufacture and various phototubes were collected using a cosmic ray test facility at Indiana University, and also at the Institute for High Energy Physics (IHEP) in Protvino, Russia, using hadron beams. The first data run at IHEP was used to test 2-m long counters with square cross sections of $2.5 \times 2.5 \text{ cm}^2$ and $5.0 \times 5.0 \text{ cm}^2$. The scintillator material was type EJ-200, produced by the Eljen Corporation. This scintillator has a decay time of 2.1 *ns*, a bulk attenuation length of 4 *m*, an index of refraction of 1.58, a peak in the emission spectrum at 425 *nm*, and a light output equal to 64% of that of Anthracene. The average time resolution measured for various combinations of scintillation bars was in the range of 100-180 *ps* for the 2.5 *cm* bars and sub-100 *ps* for the 5.0 *cm* bars, depending on the PMTs used. In a later data run 2 *m*-long bars of cross sections $2.5 \times 6.0 \text{ cm}^2$ were tested using a 5 *GeV/c* beam. Using constant fraction discriminators the time resolution for two bars was measured to be less than 40 and 60 *ps* when particle cross 6.0 *cm* and 2.5 *cm* of scintillator respectively. Based on the results presented above, therefore, we have chosen the 2.5 *cm* thick, 6 *cm* wide bar for the TOF wall.

The Čerenkov Detector

The primary function of this detector is to signal the presence of pions over a large part of the expected momentum range. The Čerenkov Detector is planned to be a gas filled threshold detector running at atmospheric pressure. Current studies suggest that a C_4F_{10} filled Čerenkov detector ($n = 1.0014$) will be a good match to the kinematics of GLUEX reactions. For individual tracks, the results of the Čerenkov detector coupled with the time-of-flight system are shown in Fig. 21.

The detector will be segmented into sixteen azimuthal regions, each housing a single mirror that focuses light onto its own photomultiplier tube. Light emitted into the region within 10 *cm* of the beam axis will not be collected in order to suppress accidental coincidences in the detector. The optical design of the detector (two ellipsoidal mirrors) was chosen to produce a strong focus at the photomultiplier tubes. This produces small linear magnification and allows good light collection from the wide range of particle trajectories exiting the solenoid. Prototype mirrors were constructed and tested for their focal prop-

erties. These were found to be mechanically and optically stable after being cut to shape. Having two mirrors in the design also offers flexibility as to the placement of the photomultipliers. This freedom will be used to place the axis of the tubes perpendicularly to the ambient magnetic field, in order to optimize the effectiveness of the passive magnetic shields surrounding the photomultipliers. A schematic drawing of the Čerenkov is shown in Fig. 22.

Because the GLUEX experiment will be reconstructing exclusive final states, perfect K - π separation for all tracks is not necessary. Detailed Monte Carlo studies using the detector parameters and imposing additional constraints such as the total strangeness in an event and kinematic fitting have been performed. We find that combining all available information will make for a very efficient particle identification system for GLUEX events.

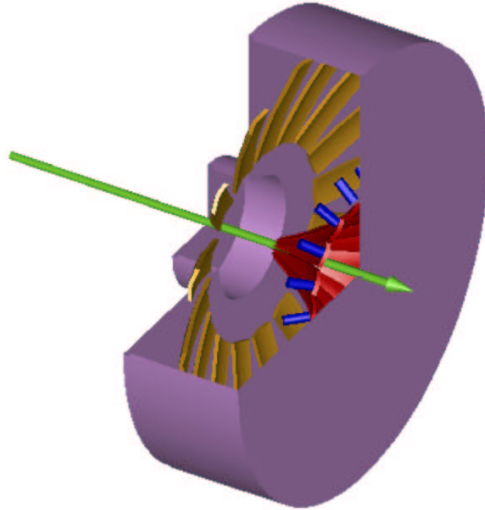


Figure 22: A schematic drawing of the GLUEX Čerenkov detector system. The beam direction is indicated with an arrow. The Čerenkov light is focused by ellipsoidal mirrors (red and orange) into phototube assemblies at the downstream side (blue cylinders).

Sub-system Installation and Integration

The assembly and integration of each of the detector subsystems into the GLUEX detector requires careful coordination and attention to many diverse issues.

The magnetic field configuration outside the magnet dictates the location and orientation of standard PMTs and/or use of hybrid PMTs. The field distribution can be affected

by magnetic materials used for support structures such as iron and, therefore, care must be taken in choosing common materials for the various support systems.

The detectors in the forward direction (Čerenkov, TOF and LGD) are relatively isolated mechanically and operate independently of other systems. The detectors inside the magnet, however, are in close proximity and mounted on the same mechanical frames that are anchored either on the BCAL or the solenoid. Therefore, cabling, power consumption, and access for maintenance must be coordinated carefully. In general, care must be exercised in the design of the electrical circuits, so as to avoid ground loops and RF interference.

The mounting and assembly of detectors must allow for the delivery of services required for their operation, including cryogenics, electrical power, ventilation, gas connections for the Čerenkov and drift chambers, as well as high voltage and signal cables for all detectors. During installation and servicing, careful surveying must be carried out to ensure a precise (better than $100\ \mu m$) knowledge of the relative tracking element location. Moreover, access to each sub-system must be facilitated for purposes of maintenance or repair.

0.B.4 Rates, Electronics, Trigger and Data Acquisition

The goal of the GLUEX readout electronics system is to digitize and read out the detector signals for level 1 trigger rates of up to $200\ kHz$ without incurring dead time. A pipelined approach is required. The digitized information will be stored for several μs while the level 1 trigger is formed. Multiple events must be buffered within the digitizer modules and read while the front ends continue to acquire new events.

Two basic types of readout electronics will be used in GLUEX, FADCs and TDCs. Detectors which measure energy will be continuously sampled with flash ADCs while detectors which require precise time measurements will use a multi-hit TDC. No currently available commercial solutions exist. These boards will be designed by our collaboration. Prototypes have been constructed, and are being tested.

The number of channels in the GLUEX detector is not large enough to justify the financially risky development of custom integrated circuits. Programmable logic devices are fast enough and available at reasonable cost. Programmable logic also allows for optimization of the data path without redesigning a printed circuit. ICs developed for other experiments could also be used. Electronics technology is constantly evolving, and the optimum solution for the GLUEX detector depends on when funding becomes available and the construction schedule.

A single channel prototype of the calorimeter FADC has been designed and built at Indiana University. A block diagram is shown in Fig. 23. A differential amplifier inverts

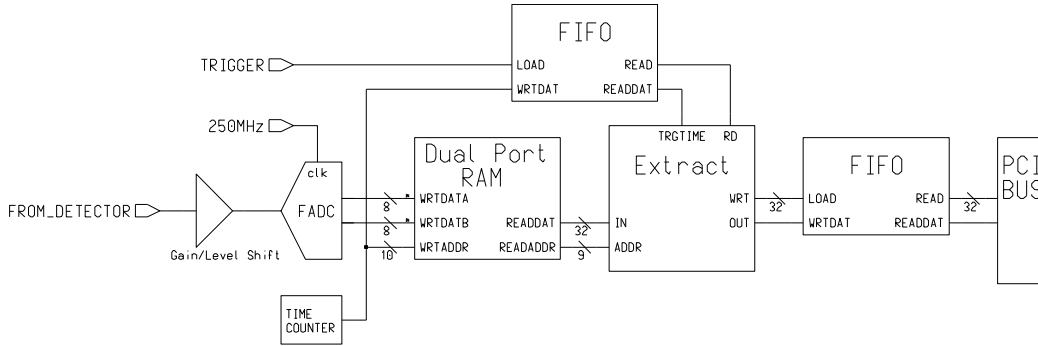


Figure 23: Block diagram of prototype FADC board.

the negative PMT signal and shifts the voltage levels to match the input range of the digitizer integrated circuit. The digitization is performed by an SPT7721 integrated circuit manufactured by Signal Processing Technologies [Spt]. This IC costs about US\$25 each in small quantities. An 8-bit value is produced internally every 4 ns; two samples are output every 8 ns (125 MHz).

All digital functions are performed in a Xilinx [Xiln] XC2S50 programmable gate array. This IC costs about US\$15 each in small quantities. A dual port RAM configured as a circular buffer stores the data for 8 microseconds. Upon receipt of a trigger signal the data from the time window of interest is copied to an output FIFO which can buffer the data from multiple events. This FIFO is interfaced to a 32 bit, 33 MHz PCI bus. More information on this prototype is available [Sm02].

The Photon Tagger, Start Counter, Vertex Tracker, Forward Drift Chamber anodes, Čerenkov Detector, Barrel Calorimeter, and Time of Flight Wall will all be read out using multi-hit TDCs. Such a high resolution pipeline TDC module has been developed for use at Jefferson Lab, and is designed to meet the requirements of current experiments, as well as to serve as a prototype for future experiments, including GLUEX. The design is implemented as a VME-64x module. This bus standard was chosen because it is already in use at Jefferson Lab, has good (and evolving) data transfer capabilities, and reasonable channel densities are possible. A block diagram is shown in Fig. 24. The module is built around the TDC-F1 integrated circuit from Acam-Messelectronic GmbH [Acam], originally designed for the COMPASS experiment at CERN [Co99].

The prototype was outfitted with a single F1 chip. All channels were found to be

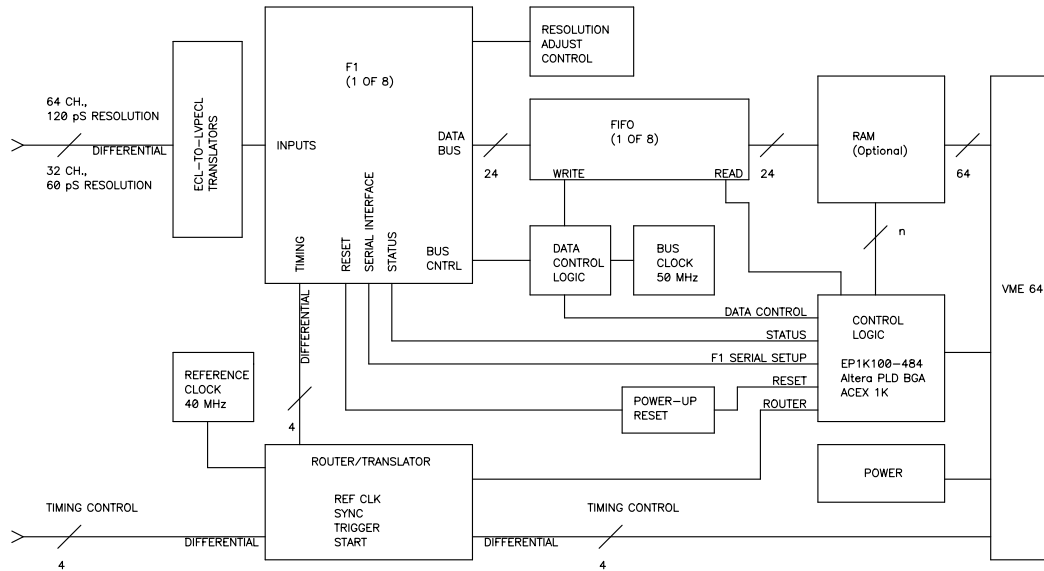


Figure 24: Block diagram of prototype TDC board.

operational and tested for performance. Timing signals were generated with a measured jitter of approximately 30 ps . The time calibration at low resolution was found to be 115.1 ps/count (120 ps/count nominal) and 57.5 ps/count in high resolution (60 ps/count nominal). Subtracting the contribution from the time generator we obtain 62 ps and 51 ps for the prototype performance in both the low and high resolution respectively. This is to be compared with the quoted rms resolution of the F1 chip of 40 ps .

Table 2 gives the total hadronic rate as well as the tagged hadronic rate for fixed electron beam conditions for various energies of the coherent peak. For $E_\gamma = 9 \text{ GeV}$ and $10^8 \gamma/s$ in the peak, the experiment will have a total hadronic rate of 365 KHz and a tagged hadronic rate of 14 KHz . Initial operating conditions will be at about 10% of these values, ($10^7 \gamma/s$), but as the the trigger improves, and the detector is better understood, rates will be pushed up toward the 10^8 number.

In order to achieve the roughly 20-1 reduction in event rate, GLUEX will use a two-stage trigger, combining a hardware-based level 1 trigger with a software (reconstruction) based level 3 trigger. An essential feature of the GLUEX design is to build pipelining into the entire trigger, digitizer, and data acquisition systems at the outset. This has the twin virtues of allowing adequate time for the level 1 trigger to do its job, while eliminating signal degradation involved in delaying the signals while the trigger operates. Pipelining in this way also allows us to upgrade from initial photon fluxes of 10^7 photons/sec to eventual fluxes of 10^8 photons/sec without any significant changes to the trigger/DAQ architecture. Eliminating conversion dead times will allow us to acquire events which occur very close together in time.

The data acquisition goal for GLUEX is to accept the level 1 trigger rate without incurring any DAQ system dead-time. The high rate of level 1 triggers (70-180 kHz) drives the design of the trigger, the front-end electronics, and the DAQ system. When the level 1 trigger is asserted, a time slice of each ring buffer will be copied, compressed and stored. Buffering will occur in groups of at least 10 event fragments on each electronic board and then transferred first across a backplane to be built into crate-event fragments and then to a computer farm to be built into complete events. The farm will perform a quick analysis to reduce the event rate by approximately a factor of ten before recording to mass storage media. This design allows GLUEX to start running with a modest tagged photon rate and then to scale-up by an order of magnitude.

The goal of the level 3 trigger is to reduce the event rate given by the level 1 trigger to an acceptable on tape rate. In low intensity running (10^7 tagged photons/s) the level 1 trigger rate is expected to be 15 kHz. Since the DAQ system is being designed to handle this rate to tape, the level 3 trigger farm will not have to cut any events, although it may be used to reduce the event rate somewhat. In high intensity mode where the level 1 rate is 70 to 180 kHz, the level 3 trigger must be able to reduce the event rate by a factor of ten.

Most of these unwanted events result from an untagged (mostly lower energy) photon interacting in coincidence with a tagged photon. Rejecting these events means that level 3 must be able to calculate, with reasonable accuracy, the energy of the photon which produced the event. This involves accurately reconstructing tracks, matching them with the calorimeter information, and adding additional energy deposited by neutral particles in the calorimeters.

Because of the accuracy requirements and the demands of linking information from different detectors, we have decided to use a processor farm architecture for level 3 instead of building a dedicated hardware processor. All events passing the level 1 trigger will be

E of peak	8 GeV	9 GeV	10 GeV	11 GeV
N_γ in peak	185 M/s	100 M/s	45 M/s	15 M/s
peak polarization (f.w.h.m.)	0.54 (1140 MeV)	0.41 (900 MeV)	0.27 (600 MeV)	0.11 (240 MeV)
peak tagging efficiency (f.w.h.m.)	0.55 (720 MeV)	0.50 (600 MeV)	0.45 (420 MeV)	0.29 (300 MeV)
power on collimator	5.3 W	4.7 W	4.2 W	3.8 W
power on target	810 mW	690 mW	600 mW	540 mW
total hadronic rate	385 K/s	365 K/s	350 K/s	345 K/s
tagged hadronic rate	26 K/s	14 K/s	6.3 K/s	2.1 K/s

Table 2: Operating parameters for an experiment using the coherent bremsstrahlung beam. The calculation assumes a 12 GeV electron beam energy and a 3.4 mm collimator 80 m downstream from a radiator of thickness 10^{-4} radiation lengths. The electron beam current is taken to be $3 \mu\text{A}$. The rates in the detector (last two rows) are calculate for a 30 cm hydrogen target and an open hadronic trigger.

read into the level 3 processor farm where they will be reconstructed; events passing the cuts applied will then be written to tape. This approach allows for algorithmic flexibility and improvements, and the ability to cost-effectively adjust to higher rates, but it does put pressure on the DAQ system.

We estimate the required processing power required as follows. The Hall B on line hit-based event reconstruction system obtains 3% momentum resolution using about 5 ms of cpu time on a 20 SPECint processor, or about 0.1 SPECint per event (full reconstruction with better than 1% resolution takes about 45 ms). Assuming the same for GLUEX gives 20000 SPECints total for the full level 3 farm at 200 KHz event rate. Assuming 50% processor utilization (due to I/O overhead, etc.), approximately 40000 SPECints or 200 processor boxes at 200 SPECint each are needed (150 SPECint boxes are currently running in the JLab farm system). Depending on the improvement in cpu performance over the next few years, far fewer boxes will likely be required, perhaps 1/4 as many.

0.B.5 Computing and Partial Wave Analysis

GLUEX will be the first Jefferson Laboratory experiment to generate petabyte scale data sets on an annual basis (One petabyte = $1 PB = 10^{15}$ Bytes). In addition, the need to generate physics results in a timely fashion has been identified as a primary goal of our collaboration since its inception. For these reasons, a well-designed, modern, and efficient

	Low Rate	High Rate
Event Size	5 KB	5 KB
Event Rate to Farm	20 KHz	200 KHz
Data Rate to Farm	100 Mbytes/s	1000 Mbytes/s
Num Links to Farm	1	10
Data Rate per Link	100 Mbytes/s	100 Mbytes/s
Link Technology	Gigabit Ethernet	Gigabit Ethernet
Events/s per Link	20000	20000
SPECints/ev for L3	0.1	0.1
Num SPECints/link	2000 SPECints	2000 SPECints
Num SPECints/link x 2	4000 SPECints	4000 SPECints
Num 200 SPECint processors/link	20	20
Total Num 200 SPECint processors	20	200

Table 3: Rates, sizes, and processing requirements for the level 3 trigger.

computing environment will clearly be crucial to the success of the experiment.

Currently, there are a number of particle physics projects world wide which also will produce very large data sets, and which will function with large dispersed collaborations. It seems quite reasonable to expect that over the coming years many new tools will be developed that will aid in effectively processing and managing these large volumes of data. As a collaboration, we will undoubtedly make effective use of these tools, which will include such things as grid middle ware, distributed file systems, database management tools, visualization software, and collaborative tools.

Nonetheless, it also is clear that the GLUEX collaboration will need to develop a suite of tools which are dedicated to this experiment. This will include data acquisition and trigger software, experiment monitoring and control software, data reduction tools, physics analysis software, and tools dedicated to the partial wave analysis (PWA) effort.

The primary goal of GLUEX is the systematic identification and categorization of short-lived meson states, unraveled from the raw, multi-particle reaction data using the techniques of PWA. Achieving this goal requires simultaneous access to two large and independent data sets, namely the actual reduced experimental data and the simulated Monte Carlo data, each sorted for the particular multi-particle reaction(s) under consideration. It

is quite probable that these data sets will be distributed physically over multiple locations, and that the access will be from other separated sites, associated with the group which has undertaken that particular analysis.

This not only impacts the structure of the data grid, but also implies that new analysis tools need to be developed. This especially includes visualization tools, as one searches for the appropriate combination of partial waves which best describe the reaction. That is, as one fits the parameters associated with a certain set of partial waves, some visual inspection mechanism is needed to evaluate how well the fit reproduces distributions in angles and invariant mass, for the many possible combinations. A universal set of tools is important in order to come to a more or less standard set of measures that would be applied by the analysis groups.

In order to identify the J^{PC} quantum numbers of a meson, it is necessary to perform a PWA. In the simplest terms, a partial wave analysis is an attempt to determine production amplitudes by fitting decay angular distributions. The fit may include information on the polarization of the beam and target, the spin and parity of the resonance, the spin and parity of any daughter resonances and any relative orbital angular momenta. The analysis seeks to establish both the production strengths and the relative phase motion between various production amplitudes. Phase motion is critical in determining if resonance production is present.

While the implementation of a PWA is in principle straight forward, there are both empirical and intrinsic difficulties. Empirically, instrumentation effects, such as detector acceptance and resolution, can conspire to make one distribution look like another. These similar distributions can lead to *leakage* from one wave into the other in the PWA. Here, cropping, smearing, or incorrect acceptance corrections of two physically different distributions may lead to distributions which are apparently indistinguishable. There is also the related problem of background in PWA. Backgrounds involve a different final state accidentally reconstructing as the channel under study. Either a particle is missed by the detector, or when putting the final state back together, multiple interpretations are possible. Both of these effects limit one's ability to measure phase motion, and can be particularly severe in a region of dense overlapping resonances. These difficulties can be minimized by properly designing the experiment. Full angular coverage in the distributions can be achieved by using a nearly 4π detector with excellent resolution. In addition, high statistics are critical to be able to accurately separate these partial waves. A thorough PWA requires nearly 4π coverage, excellent resolution, high statistics and a very good understanding of the detector.

The PWA method is subject to intrinsic mathematical ambiguities for certain final

states. Two or more different choices of amplitudes lead to identical observables. Here there are at least two approaches. The first assumes some a priori physics knowledge that allows one to choose one solution over another. The second, and cleaner approach is to simultaneously examine several final states to which the resonance can decay. While the distributions may be confused in one final state, such as $\eta\pi$, they are likely to be absent or different in a second such as $\rho\pi$. This latter approach assumes that the detector has been optimized for many different final states, and that relative normalizations between these are understood.

This latter approach of looking at multiple final states not only would allow one to separate different waves, but in itself yields key information about the relative decay rates of mesons. It is this latter information that is critical to understanding the underlying wave functions of the mesons — their content, and mixing with other states. This ability to accurately measure many final states, and perform a simultaneous PWA is a key feature of the GLUEX spectrometer for doing excellent spectroscopy.

The use of photon polarization will allow us to both simplify the analysis parameterization, as well as access additional information on the production of mesons. It will also provide key checks on the stability of the analysis itself. While circularly polarized light may yield some information in a few special cases, the true gain comes from linear polarization. Linear polarization defines a *new spatial direction* beyond the photon direction, while for circular polarization, the polarization and the momentum are in the same direction. Secondly, linearly polarized light is a coherent sum of circularly polarized light, which leads to new interference terms.

As part of the GLUEX design studies, the group has carried out a double-blind partial wave analysis on simulated data for the reaction:

$$\gamma p \rightarrow \pi^+ \pi^+ \pi^- n,$$

for 8.5 GeV photons. Studies have been done with photon polarizations ranging from 0% up to 100%. The simulated data correspond to a mix of seven waves including the a_1 , a_2 , π_2 and the $J^{PC} = 1^{-+} \pi_1$, all of which decay via $\rho^0 \pi^+$ to the 3π final state. The data are assumed to proceed via purely one-pion exchange. Two different packages for partial wave analysis have been used, each using a different formalism for fitting the data. The results between the two agree. The use of more than one analysis package on real data will allow us to better access the systematics associated with the fitting of the data. The data used in these fits corresponds to a couple percent of one year's reconstructed sample using 10^7 photons per second. It should be noted that this channel has a large photoproduction cross section, while the goal of the experiment is to simultaneously study channels with much smaller cross sections.

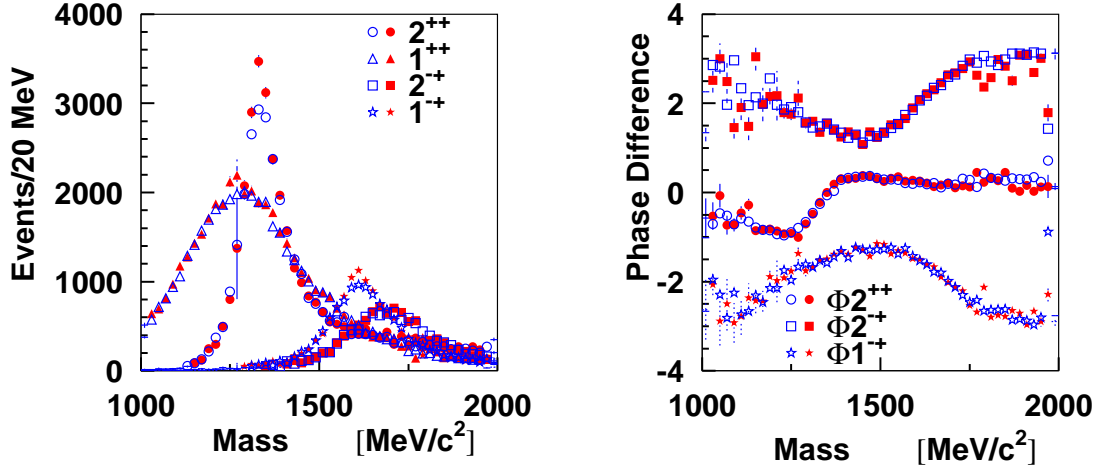


Figure 25: Partial Wave Analysis results for simulated 3π data. The solid figures correspond to generated data, while the open figures correspond to events which have been run through the GLUEX Monte Carlo program. The left hand figure shows the intensities of several waves, while the right hand figure shows the phase difference from the 1^{++} wave.

Fig. 25 shows the results of fits to the simulated data. The solid figures correspond to simple generated data, while the open figures are for data which has been run through the GLUEX Monte Carlo program to simulate both acceptance and resolution effects. The small differences between the two curves are due mostly to resolution, particularly for the fast π 's in the events. It should be noted that the 3π channel while one of the stronger photo production channels, is also one of the more difficult as far as resolution goes. The four curves correspond to the $a_2(1320)$, ($J^{PC} = 2^{++}$), the $a_1(1260)$, (1^{++}), the $\pi_2(1670)$, 2^{-+} and an exotic $\pi_1(1600)$, (1^{-+}). The phase differences are plotted with respect to the $a_1(1260)$ wave. A second PWA exercise was performed to assess the ability to extract an small exotic signal from mix of various non-exotic waves, (this latter study used simple 4-vector smearing and cuts rather than the fast Monte Carlo). Fig. 26 shows the results of this second study where the exotic wave was about 2.5 % of the total sample. The statistics shown correspond to several days of running and it is clear that one can easily extract this small signal from the data, and accurately reproduce the original resonance

Similarly, a study on the effect of linear polarization in determining the production mechanism has been undertaken. To do this, a second event generator was built that produced the same 3π final states via ρ exchange, rather than π exchange. The naturality of these two exchange particles are opposite from each other, and in the absence of linear

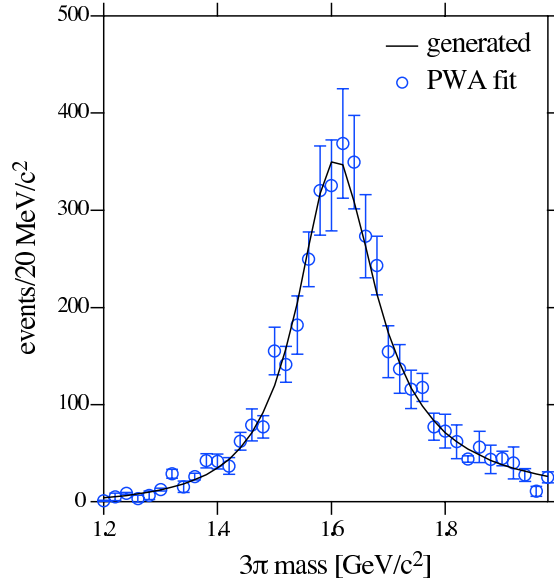


Figure 26: The results of a double-blind Monte Carlo exercise showing the $J^{PC} = 1^{-+}$ exotic wave after fitting (open circles) and the exotic wave input (curve) into the mix of $\gamma p \rightarrow \pi^+ \pi^+ \pi^- n$ events that were generated in this study. Details are given in the text.

polarization, only the sum of the two intensities can be determined. With the addition of linear polarization, it is possible to disentangle the two contributions. Fig. 27 shows this by examining the exotic 1^{-+} wave produced via both these mechanisms. The upper curves in the figures correspond to fits to the sum of the two intensities, and are well fit for all polarizations. The lower curves correspond to fits to the differences between the two intensities. This is completely undetermined for the unpolarized data set, while it is separated for the polarized samples.

A detailed *leakage* study has also been performed using the PWA tools [Za01]. In doing this, the geometry in the detector simulation for producing physics events and the detector simulation for performing the PWA were varied by several σ in the resolution parameters for the GLUEX detectors. A search was then made for signals that leaked into the exotic waves with the results that with the current detector geometry, it is extremely difficult to produce leakage into the exotic waves.

The GLUEX collaboration has organized a collaborative program with the CLEO-c experiment to develop advanced tools for PWA that would be useful for both groups. The initial efforts by GLUEX members have been to begin work on parallelizing existing PWA codes, and using these to analyze large existing data sets collected by the E852 collaboration. A sample of approximately 35-million 3π events is being analyzed using the

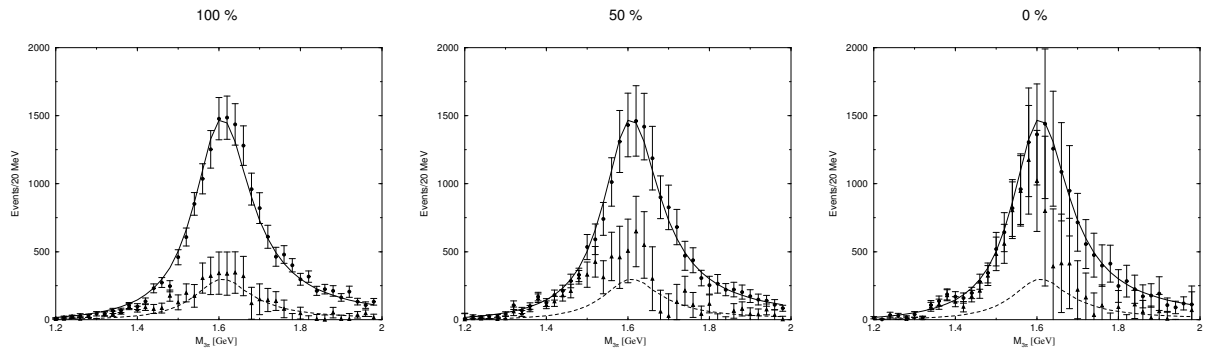


Figure 27: Partial Wave Analysis results for simulated 3π data generated with a combination of natural and unnatural parity exchanges with 100%, 50% and 0% linearly polarized photons. The upper curves correspond to the sum of the two intensities, while the lower curves correspond to the differences between the two intensities.

large computer facilities available at Indiana University. These efforts have made possible the PWA analysis of the largest data set ever.

In order to continue and expand these efforts, members of both the GLUEX collaboration and the CLEO-c collaboration submitted an NSF ITR proposal in February of 2003. This proposal would support a 4-year multi-pronged development and implementation of the next generation of PWA tool. Under this proposal, the CLEO-c contingent will develop data caching tools and interfaces to allow transparent access to large data sets. The GLUEX collaboration will work on visualization tools, parallelization of PWA code and improvements in minimization algorithms. In parallel with this, improvements in theory will be explored and implemented into the PWA tools. The tools will initially be applied to existing E852 data sets. Once CLEO-c spectroscopy data becomes available, they will be analyzed. At the end of the 4 year proposal, the goal is to have a robust set of tools that can be used to handle the GLUEX data.

0.B.6 Summary

The GLUEX beam and detector have been optimized to facilitate a robust PWA of mesons and baryons produced with an 8 to 9 GeV linearly polarized photon beam. Even with rates of only $10^7 \gamma/s$, the experiment will collect at least an order of magnitude more data than existing π beam experiments during its first year of running. Such an increase in statistics coupled with a new production mechanism will not only allow us to map out the gluonic excitations, but to measure their decay properties and production mechanisms as well.

References

- [Ab85] K. Abe *et al.* *Phys. Rev.*, **D32**:2288, 1985.
- [Ab94] K. Abe *et al.* *Phys. Rev. Lett.*, **53**:751, 1984.
- [Ab98] A. Abele *et al.* (Crystal Barrel Collaboration). Exotic $\pi\eta$ State in $\bar{p} - d$ Annihilation at Rest into $\pi^- \pi^0 \eta p_{spectator}$. *Phys. Lett.*, **B423**:175, 1998.
- [Acam] Details of the “F1” chip can be found at <http://www.acam.de>.
- [Ad98] G. S. Adams *et al.* (E852 Collaboration). *Phys. Rev. Lett.*, **81**:5760, 1998.
- [Af98] A. Afanasev and P. R. Page. Photoproduction and Electroproduction of $J^{PC} = 1^{-+}$ exotics. *Phys. Rev.*, **D57**:6771, 1998.
- [Af00] A. V. Afanasev and A. P. Szczepaniak. Charge exchange $\rho^0 \pi^+$ photoproduction and implications for searches for exotic mesons. *Phys. Rev. D*, **61**:114008, 2000.
- [Al88] D. Alde *et al.* *Phys. Lett.*, **B205**:397, 1988.
- [Am95] C. Amsler and F.E. Close. *Phys. Lett.*, **B353**:385, 1995.
- [Am96] C. Amsler and F.E. Close. Is the $f_0(1500)$ a scalar glueball? *Phys. Rev.*, **D53**:295, 1996.
- [An96] A. Antonelli *et al.*, *Nuclear Inst. and Meth. A* **370**, 367, (1996).
- [Ao93] H. Aoyagi *et al.* *Phys. Lett.*, **B314**, 1993.
- [As87] D. Aston *et al.*, *The LASS spectrometer*, Technical report, 1987, SLAC-Report-298.
- [At84] M. Atkinson *et al.* (The Omega Collaboration). *Nucl. Phys.*, **B231**:15, 1984.
- [At84a] M. Atkinson *et al.* (The Omega Collaboration). *Nucl. Phys.*, **B243**:1, 1984.
- [Ba73] J. Ballam *et al.* Vector-meson production by polarized photons from 2.8, 4.7, and 9.3 GeV. *Phys. Rev.*, **D7**:3150–3177, 1973.
- [Ba93] G.S. Bali *et al.* *Phys. Lett.*, **B309**:378, 1993.
- [Ba96] B. Baumbaugh *et al.*, *IEEE Trans. Nucl. Sci.* 43, 1146, (1996).
- [Be93] G. M. Beladidze *et al.* *Phys. Lett.*, **B313**, 1993.

- [Ba98] G. Bali *et al.* (SESAM Collaboration). *Nucl. Phys. Proc. Suppl.*, **63**:209, 1998. hep-lat/9710012.
- [Be82] B. Bengtson and M. Moszynski, *Nuclear Inst. and Meth.* **204**, 129, (1982).
- [Be96] C. Bernard *et al.* (MILC Collaboration). *Phys. Rev.*, **D56**:7039, 1997. hep-lat/9707008.
- [Bl97] G. R. Blackett *et al.* The Photoproduction of the $b_1(1235)\pi$ System. Technical report, August 1997. hep-ex/9708032.
- [Ca00] D. Cassel, F. Close, J. Domingo, W. Dunwoodie, D. Geesaman, D. Hitlin, M. Olson and G. Young, *Review of the Jefferson Laboratory "Hall D Project"*, January 2000, (http://www.phys.cmu.edu/halld/halld_notes/Note_024/).
- [Cl01] F. E. Close and A. Kirk. Scalar glueball- $q\bar{q}$ mixing above 1 gev and implications for lattice qcd. *Eur. Phys. J.*, **C21**:531–543, 2001. hep-ph/0004241.
- [Co93] G. T. Condo, T. Handler, W. M. Bugg, G. R. Blackett, M. Pisharody and K. A. Danyo. Further results from charge-exchange photoproduction. *Phys. Rev.*, **D48**:3045, 1993.
- [Co99] COMPASS experiment at CERN: <http://wwwcompass.cern.ch>.
- [Cr98] R. R. Crittenden *et al.*, *Nuclear Inst. and Meth.* **387**, 377 (1998).
- [Da73] M. Davier *et al.* The reaction $\gamma p \rightarrow \pi^+\pi^-\pi^+\pi^-p$ at high-energy and γ dissociation into 4π . *Nucl. Phys.*, **B58**:31, 1973.
- [De01] S. Denisov, *et al.*, *Timing Characteristics of SCintillator Strips*, February 2001, (http://www.phys.cmu.edu/halld/halld_notes/Note_057/).
- [Ei72] Y. Eisenberg *et al.* *Phys. Rev.*, **D5**:15, 1972.
- [Ga84] Rob Veenhof, *The GARFIELD Program, Simulation of Gaseous Detectors*, CERN, (1984), (<http://garfield.web.cern.ch/garfield/>).
- [He90] D. W. Hertzog *et al.*, *Nuclear Inst. and Meth.*, **A294**, 446, (1990).
- [Ik85] N. Isgur, R. Kokoski, and J. Paton. *Phys. Rev. Lett.*, **54**:869, 1985.
- [Is85] N. Isgur and J. Paton. Flux-tube model for hadrons in QCD. *Phys. Rev.*, **D31**:2910, 1985.

- [Iv01] E.I. Ivanov *et al.* (E852 Collaboration). Observation of Exotic Meson Production in the Reaction $\pi^- p \rightarrow \eta' \pi^- p$ at 18-GeV/c. *Phys. Rev. Lett.*, **86**:3977, 2001.
- [Ka75] W. Kaune, G. Miller, W. Oliver, R. W. Williams, and K. K. Young, *Phys. Rev.*, **D11**, 478 (1975).
- [GX02] The GLUEX Collaboration *The Gluonic Excitations experiment*, Design Report Version 4, September 2002, (http://www.phys.cmu.edu/halld/cdr_v4/).
- [La97] P.Lacock *et al.* (UKQCD Collaboration). *Phys. Lett.*, **B401**:308, 1997.
- [ML00] *Assessment of the MEGA/LASS Magnet at LANL, 20 March, 2000*, (http://www.phys.cmu.edu/halld/halld_notes/Note_026/).
- [Mo79] M. Moszynski and B. Bengtson, *Nuclear Inst. and Meth.*, **158**, 1 (1979).
- [Mo97] C.J. Morningstar and M. Peardon. Efficient glueball simulations on anisotropic lattices. *Phys. Rev.*, **D56**:4043, 1997.
- [Na70] Y. Nambu. Univ. of Chicago report No. 70-70, 1970.
- [Pe89] M. D. Petroff and M. Atac, *IEEE Trans. Nucl. Sci.* NS-36, 163, (1989).
- [Se95] J.Sexton *et al.* (IBM Collaboration). *Phys. Rev. Lett.*, **75**:4563, 1995.
- [Sm02] More information on the FADC prototype can be found at <http://dustbunny.physics.indiana.edu/~paul/hallDrd>.
- [Spt] Signal Processing Technologies: <http://www.spt.com>.
- [Sz01] A. P. Szczepaniak and M. Swat. *Phys. Lett.*, **B516**:72, 2001.
- [Th97] D. R. Thompson *et al.* (E852 Collaboration). *Phys. Rev. Lett.*, **79**:1630, 1997.
- [Wa97] M. R. Wayne, *Nuclear Inst. and Meth.* **A386**,278, (1997).
- [Xiln] Xilinx: <http://www.xilinx.com>.
- [Yu95] Yu. Prokoshkin, S. A. Sadovskii. *Phys. Atom. Nucl.*, **58**:606, 1995.
- [Za01] B. Zaroukian, J. Kaditz, C. A. Meyer and P. Eugenio, *A Study of leakage in Partial Wave Analysis for the HallD Detector at Jefferson Lab*, July 2001, (http://www.phys.cmu.edu/halld/halld_notes/Note_051/).